applied sciences

MDPI

Article

Multi-Analytical Investigation of Painting Materials on the 21st Dynasty Wooden Coffin of Ankhefenkhonsu

Giorgia Di Fusco [1,2,*], Davide Melica [3], Daniela Fico [4], Maurizio Masieri [2], Anna Consonni [5] and Giulia Germinario [2]

1 Department of Cultural Heritage, University of Salento, Via Dalmazio Birago 64, 73100 Lecce, Italy
2 Institute of Heritage Sciences-National Council of Research (ISPC-CNR), Campus Ecotekne, s.p. 6 Lecce-Monteroni, 73100 Lecce, Italy; maurizio.masieri@cnr.it (M.M.); giulia.germinario@cnr.it (G.G.)
3 Consulenza e Diagnostica per il Restauro e la Conservazione Enterprise, Via Cosimo Mariano 118, 73043 Copertino, Italy; info@diagnosticarestauro.it
4 Department of Engineering for Innovation, University of Salento, Lecce-Monteroni, 73100 Lecce, Italy; daniela.fico@unisalento.it
5 National Archaeological Museum of Florence—Ministry of Culture, Via della Colonna 38, 50122 Firenze, Italy; anna.consonni@cultura.gov.it
* Correspondence: giorgia.difusco@unisalento.it

Abstract

The study investigates the materials of the pictorial stratigraphy and the execution techniques of the 21st Dynasty anthropoid wooden coffin of Ankhefenkhonsu, belonging to the Egyptian "yellow coffins" group and preserved in the Egyptian Collection of the National Archaeological Museum of Florence. The multi-analytical approach combines non-invasive analyses—MSI and XRF—with micro-invasive analyses—PLM, SEM-EDS, ATR-FTIR (MIR-FIR), FPA-FTIR, and GC-HRMS, including Py/GC-HRMS—to characterize pigments, binders, varnish, and alteration products. The results revealed a complex and coherent multi-layered structure consisting of a coarse brown mud ground layer, followed by a fine white calcite-based preparatory layer for the application of traditional Egyptian pigments. These include a widespread yellow pictorial layer containing orpiment, Egyptian blue, a green copper-based pigment mainly identified as atacamite, red ochre, and a carbon-based pigment. The organic compounds associated with the paint layers indicate the use of plant gums, drying oils, and natural resins, suggesting the deliberate selection and combination of different organic materials during the preparation of the pictorial films. These findings provide new insights into the material selection and painting technology of the coffin, while the identification of secondary alteration products contributes to understanding the long-term transformation of its polychrome decoration.

Keywords: Egyptian coffin; in situ non-invasive analyses; high-resolution spectrometry; high-resolution FPA-FTIR imaging; painting techniques

Check for updates

Academic Editor: Ion Sandu

Received: 24 September 2026
Revised: 15 October 2026
Accepted: 17 October 2026
Published: 23 October 2026

Copyright: © 2026 by the authors. Licensee MDPI, Basel, Switzerland. This article is an open access article distributed under the terms and conditions of the Creative Commons Attribution (CC BY) license.

1. Introduction

The polychrome wooden coffin of Ankhefenkhonsu (n. inv. 48523/ME8523), part of the Egyptian collection of the National Archaeological Museum in Florence [1], belongs to the group of so-called Egyptian "yellow coffins" [2–5], a specific class of artifacts that appeared in Thebes toward the end of the New Kingdom (1550-1069 BCE) and remained in use for over a millennium, reaching their peak during the 21st Dynasty (ca. 1069–945 BCE).

These coffins (Figure 1) are known as "yellow" coffins due to their distinctive background color, which was meant to evoke the appearance of gold. They take an anthropoid

shape, with finely detailed faces and hands, and include features that indicate the gender of the deceased. A defining characteristic of these coffins is the varnished surface laid over a vividly colored decorative program, marked by a strong *horror vacui*, with every available space densely filled with decorations.



Figure 1. The polychrome wooden coffin of Ankhefenkhonsu.

The evolution of this coffin type has been, and continues to be, widely studied, particularly because of the large group uncovered in the 19th century in the Bab el-Gasus cache—where the present coffin also comes from—which are now scattered across museums around the world [6].

The Bab el-Gasus cache was discovered in January 1891 at Deir el-Bahari, in the Theban necropolis. It consisted of galleries containing over 200 coffins and other grave goods belonging to the Priests of Amun, dating to the 21st and early 22nd Dynasties. The Giza Museum retained part of the coffins, while the rest was divided into lots and distributed to countries involved in diplomatic relations with Egypt. Seventeen lots were assigned: Italy received "Lot V," which was sent to Florence in 1893 thanks to the strong relationship between the then Director of the Egyptian Museum in Florence, Ernesto Schiaparelli, and the Ministry of Public Education [7].

The yellow coffins formed part of a nested funerary assemblage, typically consisting of one or two coffins with their corresponding lids and cases. A larger outer coffin enclosed an inner coffin that contained the mummified body of the deceased. The assemblage of yellow coffins also included a third element, the mummy board: a flat and small version of the lid placed directly over the mummy.

The coffin here examined is an outer coffin of a set [8] preserving an inner one (n. inv. 48526/ME8526) and a mummy board (n. inv. 48521/ME8521).

According to the recent studies of Kathlyn M. Cooney, all the coffins held in the Museum of Florence and found in Bab el-Gasus show traces of reuse [9], a practice that became widespread during the 21st Dynasty due to the social crisis at the end of the New Kingdom and the resulting scarcity of materials [10,11].

The set to which the coffin of Ankhefenkhonsu belongs remains anonymous. The outer lid displays male features, and the name Ankhefenkhonsu—its original owner—is

written in red on the case. By contrast, the inner coffin, which is considerably earlier, shows female features. The mummy cover was originally made for a male individual but was later modified with female attributes, including earrings and open hands. The inscriptions on the mummy board bear the name Ankhesenmut.

The coffin was constructed from planks of wood, with face and hands carved separately and then attached to the main structure. To connect the different parts, a large variety of joints was used. Analyses of the lid indicate that the boards were made of *Ficus sycomorus*, while the pegs were crafted from *Tamarix* sp. [12].

The wooden structure was covered by layers of paste, each differing in granulometry and composition, upon which the decoration was applied, with the occasional use of the *pastiglia* technique, a low-relief decoration obtained by applying a plaster-based paste directly onto a wooden surface, which is then decorated.

The lid of the coffin is decorated exclusively on its exterior, featuring a finely modeled face painted yellow, traces of a collar and pectoral and crossed fists originally holding large amulets. The central decorative program is arranged in symmetrical horizontal registers and longitudinal sections, combining painted details and modeled elements. Recurring motifs include scarabs with solar disks, Osiris and Isis, winged protective goddesses, sacred animals, mummiform deities, and apotropaic symbols, alongside ritual scenes of offerings, libations, and purification. Five longitudinal inscriptions, outlined in red above a yellow background, with motifs in blue, green, and red, run along the lid.

The coffin case is decorated on both its interior and exterior. The exterior features multiple registers of cobras, green feathers, hieroglyphic inscriptions, and symbolic and ritual scenes, including the Ta-wer totem, Osirian motifs, the sacred boat, and the sacred cow emerging from the Theban Mountain. The interior, painted red with yellow edges, displays the deceased's ba-soul beneath the sky sign on the headboard, flanked by sacred cobras, symmetrical registers of mummiform deities on the sides, and Osiris, the solar disk, and other divine motifs on the floorboard.

This coffin set was discovered in the main gallery of Bab el-Gasus, next to the western wall, lying beneath another coffin, a circumstance that may also account for the poor state of preservation of the outer coffin. The lid is severely damaged, with extensive losses of paste and pictorial layers, particularly in the wig and facial areas; the right ear and beard are no longer preserved. A prominent longitudinal fracture runs along the central axis of the case, from the fists to the footboard, while further losses affect the lower section and much of the footboard. The case is marked by multiple fractures across its entire surface, and the external decoration of the sidewalls is heavily compromised, especially at the headboard. Although the interior also exhibits widespread cracking, the painted decoration remains comparatively well preserved.

The restoration, carried out by Croma Srl (Conservazione e Restauro Opere e Monumenti d'Arte, Rome), was deemed necessary due to the precarious state of the coffin, which threatened both its structural stability and the legibility of its decoration. To guide conservation and to characterize painting materials and the execution technique, the coffin was subjected to non-invasive—Multispectral Imaging (MSI) and X-ray Fluorescence (XRF)—and micro-invasive analyses.

To characterize the stratigraphic sequence and the pictorial materials, some microsamples were analyzed in cross-section with Polarized Light Microscopy (PLM), Scanning Electron Microscopy–Energy Dispersive X-ray Spectroscopy (SEM-EDS) and Focal Plane Array–Fourier-Transform Infrared (FPA-FTIR) imaging. In addition, the use of the Attenuated Total Reflectance–Fourier-Transform Infrared Spectroscopy (ATR-FTIR) aimed specifically to identify the kind of pigments. Moreover, to identify the varnish, organic binders and materials, the samples were first analyzed with Pyrolysis/Gas Chromatography–High

Resolution Mass Spectrometry (Py/GC-HRMS) and on the basis of the results, GC-HRMS was also performed to better specify the nature of the binders.

These analyses will contribute to expanding the knowledge on this coffin type, particularly in light of the growing scholarly focus on production processes, raw materials, and painting techniques [13–16].

2. Materials and Methods

2.1. Non-Invasive Analyses

Non-invasive analyses were extended on the lid (external side) and the case (external and internal sides).

2.1.1. Multispectral Imaging (MSI)

The analysis was conducted with a Sony Cybershot DSC F828 camera equipped with a CCD sensor chip of 8 Mpx; this model presents a built-in NightShot function, which allows the exclusion of the thermic filter within the photo camera without any mechanical adjustments. A filter RGBE differs from classic RGB due to the addition of cyan in the filter mosaic mounted in front of the sensor. Unlike the Bayer matrix sensor, where two green filters, one red, and one blue, cover an area of four photodiodes, in this case, there are one green, one red, one blue, and one filter of a color similar to cyan (emerald). The lens is fixed and features a 28 to 200 mm optical zoom.

As radiation sources, two halogen lamps 400 W were used for documenting in the visible range and near-infrared (NIR), and two Wood lamps (with 50 W of power, a spectral region of 300–400 nm and a peak emission of 365 nm) for the photographic documentation in the UV range.

Different modalities of acquisition are shortly described in the following:

- Visible-light photography (VIS);
- Infrared photography (IR): a B+W 850 filter was mounted in front of the lens.
- Infrared False-Color Image Processing (IR-FC): This method is based on uniting different components within a single image, the signal from an infrared band with that from selected bands of the visible spectrum and assigning colors that differ from their natural appearance. Specifically, the green component from the visible range (500–600 nm) is replaced by the color blue, and the red component from the visible range of the spectra is replaced by the color green, while the component from the near-infrared range (700–900 nm), obtained with IR, is assigned to the color red. The blue component from the visible range (400–500 nm) is excluded from the false color image processing. In this color shift, the infrared component is shown in red, while information from part of the visible spectrum is simultaneously preserved. As a result, pictorial layers that are chromatically similar but contain pigments with different chemical compositions can be distinguished. In some cases, it could be possible to identify or at least hypothesize the presence of certain pigments as their chemical composition causes them to interact differently with various visible and infrared wavelengths.
- Ultraviolet Fluorescence Photography (UVF): Some organic compounds are fluorescent when exposed to UV radiation. This property is useful for compound differentiation and characterization, evaluation of their state of preservation and documenting possible previous interventions. Photographic documentation of fluorescence was performed using two Wood lamps and a B+W 420 filter mounted in front of the camera lens. The filter was used to attenuate the UV radiation reflected from the surface of the artwork and the violet light at wavelengths below 420 nm, allowing the recording

of visible fluorescence. Images were acquired with an exposure time of 4 s, an ISO setting of 200, and an aperture of f/11.3.

2.1.2. X-Ray Fluorescence (XRF)

Elemental chemical analysis was conducted with a portable device Bruker S1 Titan 800, equipped with a generator of X-rays with a rhodium (Rh) anode, which allows the detection of chemical elements from magnesium (Z = 12) to uranium (Z = 92), using the following experimental conditions: tube voltage 15 kV, tube current 45 μA, and exposure time 60 s.

XRF points of analysis were extended on the blue, black, brownish, red, yellow and green areas (Supplementary Figures S1–S7).

2.2. Micro-Invasive Analyses

A limited number of micro-samples were taken from the different colored areas of the coffin lid, while additional unlocated samples were already available from the internal coffin case. Figure 2 shows the areas of the samples taken, and Table 1 reports the list, the description of the samples and the relative analyses performed.



Figure 2. Overview of the sampling locations and corresponding detailed views (highlighted in red).

Table 1. List and description of the coffin's samples involved in the diagnostic campaign and the related analyses.

ID	Description	Sampling Area	Analyses
SF1	Yellow pictorial layer with a yellow varnish	Lid—right hand	PLM, SEM-EDS, ATR-FTIR (FIR), Py-GC-HRMS
SF2	Yellow and blue pictorial layer	Lid—head	PLM, SEM-EDS, ATR-FTIR (FIR), Py-GC-HRMS
SF3	Yellow pictorial layer	Lid—left hand	PLM, SEM-EDS, ATR-FTIR (FIR), Py-GC-HRMS

Table 1. *Cont.*

ID	Description	Sampling Area	Analyses
SF4	Yellow and blue pictorial layer	Lid—head	PLM, SEM-EDS, ATR-FTIR (FIR), Py-GC-HRMS
SF5	Green pictorial layer	Erratic fragment from internal base	PLM, SEM-EDS, FPA-FTIR, ATR-FTIR (MIR-FIR), Py-GC-HRMS
SF6	Blue pictorial layer	Erratic fragment from internal base	PLM, SEM-EDS, ATR-FTIR (FIR), Py-GC-HRMS
SF7	Yellow pictorial layer	Erratic fragment from internal base	PLM, SEM-EDS, ATR-FTIR (FIR), Py-GC-HRMS
SF8	Yellow pictorial layer	Erratic fragment from internal base	PLM, SEM-EDS, ATR-FTIR (FIR), Py-GC-HRMS
SF9	Blue-yellow-red pictorial layer	Erratic fragment from internal base	PLM, SEM-EDS, FPA-FTIR, ATR-FTIR (FIR), Py-GC-HRMS

2.2.1. Polarized Light Microscopy (PLM)

The samples were embedded in polyester resin and polished until a mirror-like surface was achieved in order to obtain polished cross-sections. To prepare the thin cross-sections, after embedding in resin and polymerization, the samples were mounted on a glass slide, cut, and reduced to a thickness of approximately 30 µm by lapping. Observations were performed using a Nikon Eclipse 100N LV POL polarized-light optical microscope (Nikon Europe B.V, Amstelveen, The Netherlands), under visible and UV light in the transmission and reflection modes, using the mutual orientation of the polarizers. Microphotographs were acquired with a Nikon DS-Ri1 camera (Nikon Europe B.V, Amstelveen, The Netherlands) controlled by Nikon NIS-Elements AR imaging software after focusing the microscope at the selected magnification. The corresponding magnification was specified in the software to ensure accurate scale bar calibration. White balance (autowhite) was adjusted to ensure faithful color reproduction. The examination aimed to characterize the stratigraphic sequences, document the features of individual pictorial layers, and identify components distinguishable by their optical properties.

2.2.2. Scanning Electron Microscopy–Energy Dispersive X-Ray Spectroscopy (SEM-EDS)

The polished cross-sections were examined using a Zeiss EVO 15 scanning electron microscope (Zeiss, Jena, Germany) fitted with a tungsten filament. Analyses were performed under low-vacuum conditions (90 Pa), without applying a conductive coating. Depending on the samples, the accelerating voltage was set to either 25 or 30 KeV; the instrument has a reported resolution of 3.4 nm. Elemental characterization was carried out by acquiring EDX spectra and elemental distribution maps. The image scan size was set to 512 pixels along the x-axis, with an energy range of 10 KeV, 1024 channels, and an acquisition time of 20 s. Elemental maps were collected using five frames, a pixel dwell time of 1 ms, and a process time of 4. EDX analyses were performed using the AZtec 6.0 SP1 software platform version and an UltimMax 40 mm2 SDD detector (Oxford Instruments, Abingdon, UK), with a resolution of 127 eV FWHM @MnK, a detection limit of about 0.1 wt% from 0.3 to 3 µm in depth, and a standardless ZAF quantification system (AutoPhaseMap mode).

2.2.3. Attenuated Total Reflectance–Fourier-Transform Infrared Spectroscopy (ATR-FTIR)

ATR-FTIR Mid-Infrared (MIR) and Far-Infrared (FIR) measurements were carried out using a Bruker INVENIO® FT-IR spectrometer (Bruker Optics GmbH, Ettlingen, Germany) fitted with an Attenuated Total Reflectance (ATR) accessory featuring a wide-range

monocrystalline diamond crystal. Spectra were acquired over the 4000–80 cm^{-1} range, at a resolution of 4 cm^{-1}, with 100 scans per measurement. The instrument configuration enables continuous coverage of both MIR and FIR regions in a single measurement without manual component swapping. This is achieved through a broadband multimode beam splitter covering 6000–80 cm^{-1} and a broad-range DLaTGS detector equipped with a specialized polyethylene (PE)/diamond window, which operates without liquid-nitrogen cooling. Background spectra were collected in air before sample spectral images. No ATR depth-of-penetration correction was applied to the acquired spectra. This choice was based on the primarily qualitative purpose of the analysis, which focused on the identification of pigments and binders through their molecular fingerprints. The positions of characteristic absorption bands (cm^{-1}) are not affected by wavelength-dependent penetration depth. Furthermore, the analyzed micro-samples were heterogeneous, with potentially substantial variations in refractive index (n_2). Applying a standard correction based on an assumed constant refractive index could therefore introduce spectral distortions. The resulting spectra were processed using OPUS-IR™ software (version 7.5; Bruker Optik GmbH, Ettlingen, Germany), and interpreted by comparison with uncorrected ATR reference spectra from databases, including the Infrared and Raman Users Group (IRUG) spectral database, and with data reported in the scientific literature.

2.2.4. Focal Plane Array–Fourier-Transform Infrared (FPA-FTIR) Imaging

FPA-FTIR imaging was carried out to investigate the distribution and chemical nature of pigments and binders in polished sample cross-sections. Measurements were performed using a Lumos II FT-IR micro-spectrophotometer (Bruker Optics GmbH, Ettlingen, Germany) fitted with a microscope and a liquid-nitrogen-cooled Focal Plane Array (FPA) detector comprising 32 × 32 elements. The instrument was equipped with an attenuated total reflection (ATR) germanium crystal. Data were collected in reflection mode over the 4000–750 cm^{-1} spectral range, at a spectral resolution of 4 cm^{-1}. Each image consisted of 1024 individual spectra acquired from an area of approximately 150 × 150 μm^2, using 64–200 scans. Each spectrum provided molecular information from a sample area of approximately 5 × 5 μm^2. Background spectra were recorded on a gold mirror before the acquisition of each sample image. The resulting datasets were processed using OPUS-IR™ software (version 7.5; Bruker Optik GmbH, Ettlingen, Germany), and spectral assignments were made by comparison with reference databases and the published scientific literature.

2.2.5. Pyrolysis/Gas Chromatography–High Resolution Mass Spectrometry (Py/GC-HRMS)

Py/GC-HRMS analyses were carried out after separating with a scalpel under a stereomicroscope the different layers, although, for some samples, it was not possible to separate them due to their small thicknesses. For the Py/GC-HRMS analyses, few mg of samples were analyzed with and without derivatization. The samples were derivatized with 5 µL of tetramethylammonium hydroxide (TMAH) in aqueous solution at a concentration of 2.5% by weight (Sigma-Aldrich, Saint Louis, MO, USA) for 1 h at 70 °C. 1 µL of the derivatized sample was placed into a stainless-steel cup and inserted into the microfurnace at a temperature of pyrolysis of 500 °C. All samples were first analyzed with Py/GC-HRMS to determine the main classes of chemical organic compounds present in the different layers.

2.2.6. Gas Chromatography–High Resolution Mass Spectrometry (GC-HRMS)

On the basis of the Py/GC-HRMS results, two fragments of the blue pictorial layer belonging to the sample SF6 were subjected to two different procedures for determining the lipidic and polysaccharide fractions of the binder. The procedures were performed with

some modifications of the combined procedure proposed by previous studies for the lipidic fraction [17] and for the carbohydrate fraction [18]. This modification was implemented following tests with different standards (fatty acid solution and monosaccharide solution), which demonstrated improved efficiency without contamination.

Both procedures involve prior extraction with 200 µL of 2.5 N ammonia in an ultrasonic bath at a temperature of 60 °C for 120 min (twice).

2.3. Lipidic/Resin Extraction Procedure

The ammonia extract was evaporated to dryness under nitrogen and hydrolyzed with 200 µL of 6 N HCl at 110 °C overnight. After cooling, 200 µL of bidistilled water were added and the solution was extracted three times with 200 µL of diethyl ether. The organic phase was combined with the residue from the initial ammonia extract, dried under nitrogen, and saponified with 300 µL of 10 wt% KOHEtOH at 70 °C for 120 min. The saponified mixture was diluted with bidistilled water, acidified with a 1:1 aqueous solution of trifluoroacetic acid, and extracted three times with diethyl ether and three times with n-hexane, yielding the lipid–resinous fraction. Five microliters of tridecanoic acid (internal standard) were added, and the extract was dried under nitrogen and derivatized with 20 µL of BSTFA containing 1% trimethylchlorosilane and 50 µL of isooctane at 60 °C for 30 min. After addition of 100 µL of isooctane and 10 µL of tetratriacontane (injection standard), 1 µL of the final solution was injected for GC-HRMS analysis.

2.4. Carbohydrate Extraction Procedure

The ammonia extract was evaporated to dryness under nitrogen, and mannitol was added as internal standard to reach 20 ppm in the injection volume. Then, 100 µL of 1.2 M trifluoroacetic acid were added, the vial was purged with nitrogen for 30 s, and hydrolysis was performed in a sealed conical vial at 125 °C for 1 h. The vial was allowed to cool to room temperature. Fifty microliters of o-methoxylamine hydrochloride in pyridine (20 mg/mL) were added, and the mixture was heated at 70 °C for 20 min. After cooling, 50 µL of BSTFA were added and derivatization proceeded at 30 °C for 45 min. One microliter of the final solution was injected for analysis.

2.5. Operative Conditions

Analyses were performed using a TRACE™ 1310 GC system (Thermo Fisher Scientific S.p.A., Rodano, Milan, Italy) equipped with a TG-5 SILMS capillary column (30 m × 0.25 mm, 0.25 µm film thickness) and helium (99.999%) as carrier gas. The GC was coupled to a Q Exactive™ (Thermo Fisher Scientific, Bremen, GmbH, Germany) operated in EI mode at 70 eV with a 50 µA emission current. High-resolution spectra were acquired at 60,000 FWHM (m/z 200). Data acquisition and processing were carried out using X-Calibur 4.0 and TraceFinder 4.1.

2.6. Pyrolysis-GC-HRMS

Pyrolysis was conducted using a Multi-Shot Pyrolyzer™ (EGA/PY-3030D, Frontier Laboratories Ltd., Koriyama, Japan) with Auto-Shot Sampler™ (AS-1020E, Frontier Laboratories Ltd., Koriyama, Japan). Samples were pyrolyzed in single-shot mode at 550 °C for 20 s. The pyrolyzer interface was maintained at 300 °C, and the GC injector at 280 °C. Carrier gas flow was set at 1 mL/min. The GC oven program was: 40 °C (2 min), ramp 10 °C/min to 320 °C, final hold 5 min. The MS transfer line and ion source were set at 250 °C and 260 °C, respectively. Full-scan acquisition (profile mode) was performed over m/z 40–550.

2.7. GC-HRMS of Polysaccharide Fraction

The oven program was: 80 °C (1 min), ramp 2.5 °C/min to 170 °C (15 min), then 20 °C/min to 280 °C (10 min). The PTV injector was set at 280 °C, with helium flow at 1.2 mL/min. The MS transfer line was maintained at 250 °C and the ion source at 280 °C. A solvent delay of 10 min was applied. Full-scan data were acquired over m/z 40–650.

2.8. GC-HRMS of Lipid Fraction

The oven program was: 80 °C (2 min), ramp 10 °C/min to 200 °C (3 min), then 10 °C/min to 280 °C (3 min), and finally 20 °C/min to 300 °C (30 min). The PTV injector temperature was 300 °C, with helium flow at 1.2 mL/min. The MS transfer line was set at 280 °C and the ion source at 300 °C. Full-scan acquisition was performed over m/z 50–750.

2.9. Data Processing

Chromatograms and pyrograms were acquired using X-Calibur 4.0 and processed in TraceFinder 4.1. Pyrograms were deconvoluted using the TraceFinder Deconvolution Plugin to perform semi-quantitative evaluation of compounds associated with specific organic binders across stratigraphic layers. Peaks identified with high confidence were integrated using the m/z values assigned during deconvolution.

3. Results

3.1. Non-Invasive Analyses

Imaging in the Visible (VIS), Infrared Reflectography (IR), Infrared False-Color (IR-FC) and the UV Fluorescence documentation (Figure 3) allow us to obtain information about the underdrawing and the execution technique. Regarding the identification of pigments obtained by IR-FC images, the use of the XRF technique allows us to obtain a more accurate interpretation on the basis of elemental chemical analysis.

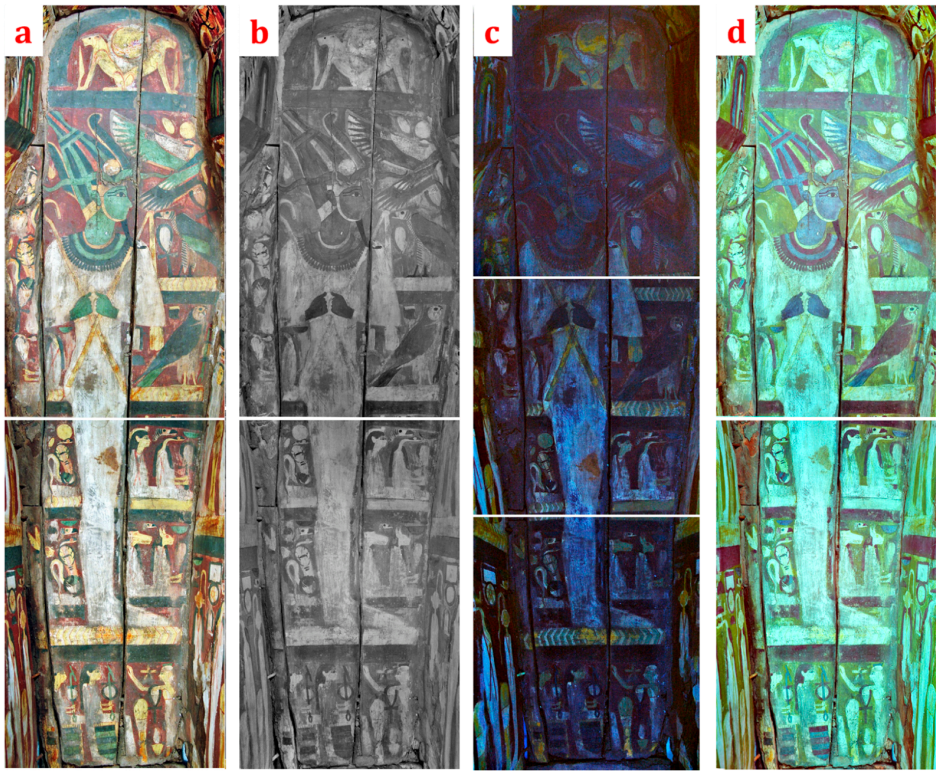


Figure 3. Visible (**a**), Infrared Reflectography (**b**), Infrared False-Color (**c**) and UV Fluorescence (**d**) images of the coffin, internal surface.

The red underdrawing (Figures 3 and 4) was realized with brushstrokes of red ochre, defining the contours of the figure; in some parts, they are very thin, as in the case of the somatic features. It is clearly recognizable to the naked eye, while in the IR imaging it is completely transparent. The contours of the figures painted in black maintained the coloration also in IR images (Figures 3b and 4b), this behavior confirming the use of carbon-based pigments [19]. Infrared photographic documentation detects with detail large brushstrokes used for the execution of painted surfaces.

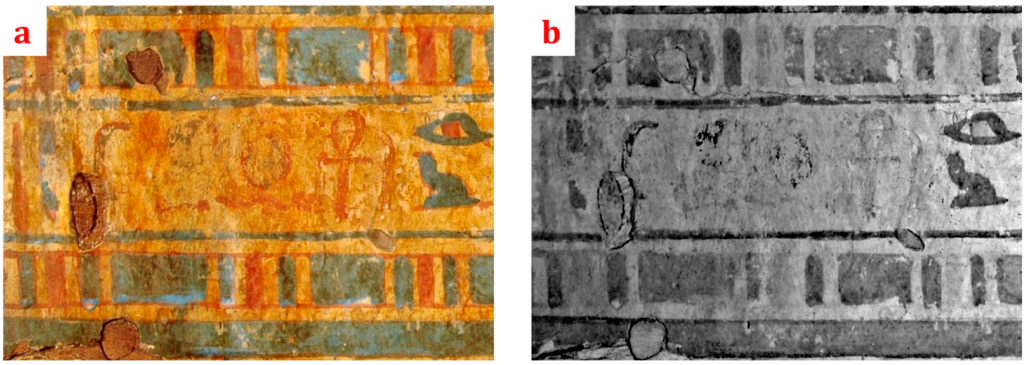


Figure 4. Visible (**a**) and Infrared Reflectography (**b**) images of the coffin, external surface, and detail of the name of the deceased with traces of previous inscription.

Visible fluorescence imaging detected a varnish layer, heterogeneously distributed across the painted surface, characterized by yellow emission typical of some natural resins. This effect has already been observed on red and yellow areas of other paintings, perhaps to create a brilliant effect simulating the gold [20].

It is important to note that the correspondence between a pigment, or a mixture of pigments, and the associated false color is not always univocal, as it can be influenced by the concentration and purity of the pigments, as well as by the presence of altered restoration fixatives. For this reason, the photographic investigations were supplemented with XRF analyses (Table 2) [21–25]. The blue bands and discs are highly likely to contain Egyptian blue, as indicated by the consistent presence of copper, calcium, and silicon, which are the main elements constituting the crystal structure of cuprorivaite [26,27]. The red discs, dark background, and flesh tones, on the other hand, appear to have been painted with red ochre, as suggested by the predominance of iron oxide. The green-painted areas contain copper-based pigments, probably malachite. However, the concomitant presence of chlorine may indicate alteration of the original copper-based pigment and the formation of atacamite/paratacamite as a degradation product [26]. In correspondence with the white ground areas, the detection of calcium as a major element and sulfur in minor amounts suggests the presence of calcium carbonate, occasionally associated with minor amounts of gypsum. The yellow areas exhibit traces of arsenic, which may indicate the use of orpiment [28,29]. The black drawings do not show any chemical elements other than calcium. Therefore, in the absence of specific inorganic elemental markers, these areas are considered likely to contain carbon-based pigments of vegetal origin [26,28]. Finally, the brown headpiece is characterized by a high copper content, which cannot be readily associated with a copper-based pigment producing such a coloration. Previous studies have suggested that the Egyptian blue may undergo darkening under certain environmental or alteration conditions, potentially accounting for the observed brownish appearance [30,31].

Table 2. List of the areas investigated with non-invasive analyses, relative pigments and inorganic materials identifiable.

VIS	IR-FC	XRF [1]	Possible Pigments End Extenders [1]
Dark red	Yellow	Ca*, **Fe***, Al*, Si*, S, K, Ti, Mn, Ni, Cu, As (point 2)	**Red Ochre**, Calcite
Dark blue	Fuchsia, violet	**Cu***, Ca*, Fe, Al, Si, Pb, S, K, Ti, Mn, Ni, Sn, As (point 1)	**Egyptian blue**
Green	Bluish	**Cu***, Ca*, Cl*, S*, Fe, Si, P, K, Ti, Mn, Ni, As, Sn (point 16)	**Copper-based pigments**, calcite, gypsum
Yellow	Light yellow	Ca*, **S***, Fe, **As***, Al, Si, K, Ti, Ni, Cu (point 6)	**Orpiment**/**Realgar**, calcite
Black	Black	Ca*, Fe, Mg, Al, Si, P, S, K, Ti, Mn, Ni, Cu (point 9)	**Carbon-based pigment**, Calcite

[1] The asterisk after the chemical element symbol meaning the major elements detected. The text formatting (bold and underline) indicates the proposed correspondence between detected elements and possible pigments and extenders, as well as underlying preparatory layers that may have contributed to the XRF signal. The points of XRF analyses are shown in Supplementary Figures S1, S4, S5 and S7.

3.2. Micro-Invasive Analyses

The optical microscopic observations reveal a composite stratigraphy common to all examined samples. This sequence includes a varnish layer, colored pictorial layers, a white preparatory layer, and a brown ground layer.

The **varnish layer**: The yellow samples (Figure 5, a) from the yellow background of the coffin show a thick layer, up to about 70 µm, that is deep brown in visible light and yellowish under UV light.

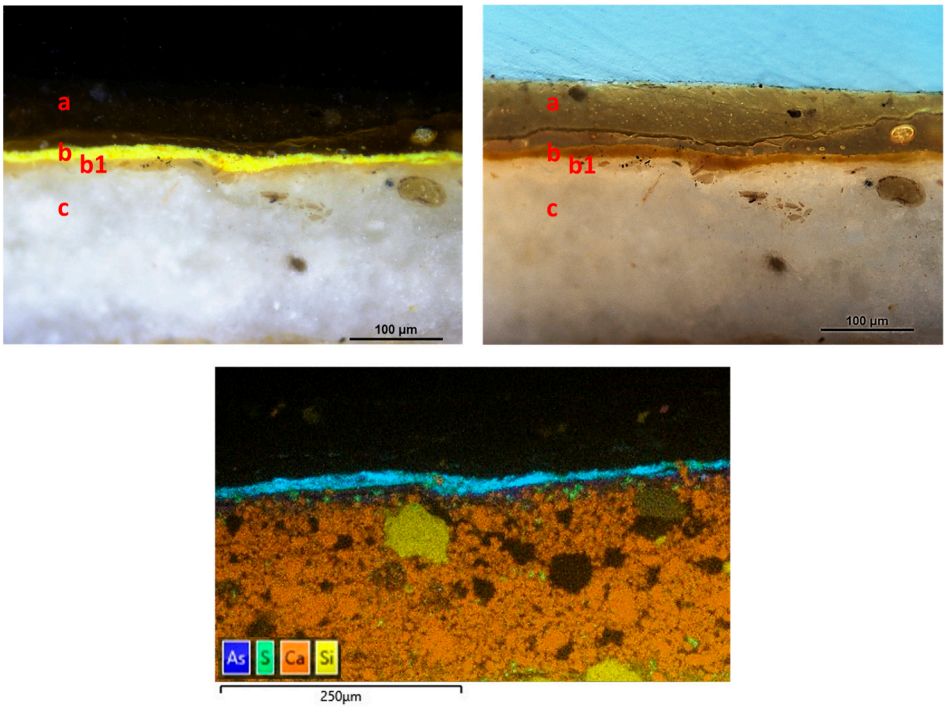


Figure 5. Sample SF1 stratigraphy observed on polished cross-section under PLM with VIS light (**top left**) and UV light (**top right**), along with an SEM-EDS map of the main elements detected in the same area (**on the bottom**).

The Py/GC-HRMS data (Supplementary Table S1) suggest the use of a *Pistacia* resin recognizable by the detection of 22,23,24,25,26,27-hexakisnor-dammaran-3,20-dione, 20,24-epoxy-25-hydroxy-dammaran-3-one, moronic acid, and oleanolic acid. Few samples reveal two isomers of 28-norolean-17-en-3-one and 28-norolean-18-en-3-one, can be due to a thermal alteration of this resin [32].

Sandaracopimaric acid, isopimaric acid and dehydroabietic acid, ascribable to a conifer resin, can be detected in all samples, sometimes together with characteristic monoterpenes [33].

In addition, different saturated fatty acids (up to C25), unsaturated acids (C16:1 and C18:1), and dicarboxylic acids (butanedioic acid, pentanedioic acid and nonanedioic ac-id) suggest the presence of an oxidized drying oil component. To better understand the nature of the lipidic fraction, one sample (sample SF6: blue and yellow pictorial layer + varnish layer) was also subjected to the lipidic procedure, confirming the presence of a complex mixture of lipidic and resinous compounds. The identified fatty acids included nonanoic acid (C9:0), tetradecanoic acid, pentadecanoic acid isomers, hexadecanoic acid (palmitic acid), and octadecanoic acid (stearic acid), together with dicarboxylic acids such as nonanedioic acid (azelaic acid), hexanedioic acid (adipic acid) and dodecanedioic acid. In addition, several monoacylglycerols were detected, including 2-palmitoyl glycerol, 1-monopalmitin, 2-monostearin, and glycerol monostearate. These compounds are consistent with the degradation and oxidation products of a lipidic binding medium, most likely a drying oil [17].

The chromatographic profile also confirmed the presence of dehydroabietic acid, a diagnostic marker of diterpenoid resin materials derived from conifer resins, such as rosin or colophony. Furthermore, the detection of β-amyrin and 24-noroleana-3,12-diene indicates the presence of a triterpenoid natural resin, possibly *Pistacia* resin, likely associated with varnish. Benzoic acid and salicylic acid were additionally identified: these compounds may derive from secondary oxidation processes, degradation of aromatic resin components, or later conservation treatments (Figure 6).

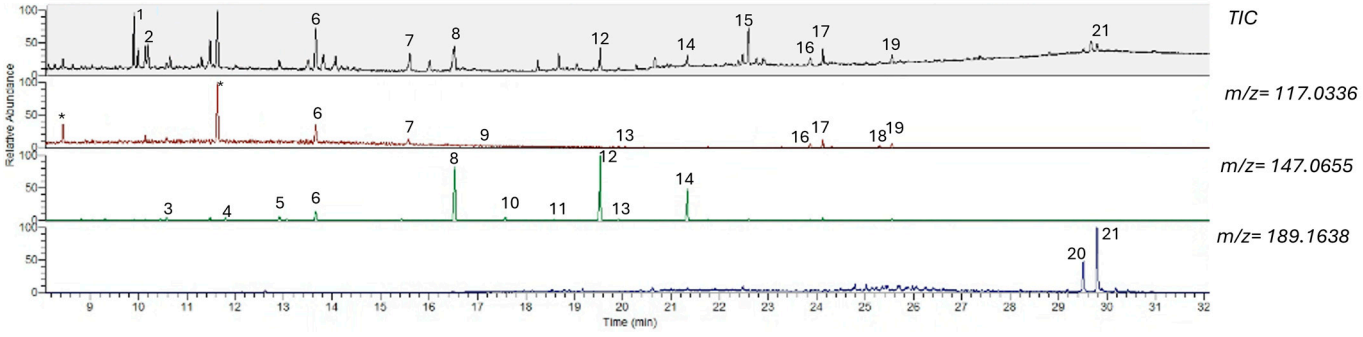


Figure 6. TIC and EIC chromatograms relative to m/z = 117.0336 for fatty acids; m/z = 147.0655 for dicarboxylic acids; and m/z= 189.1638 for triterpenoid resins. Legend: 1. benzothiazole; 2. benzoic acid; 3. propylene glycol; 4. nonadecanoic acid; 5. adipic acid; 6. hexanedioic acid, 7. salicylic acid; 8. tridecanoic acid (IS); 9. nonanedioic acid; 10. tetradecanoic acid; 11. pentadecanoic acid (x3 isomers); 12. hexadecanoic acid; 13. dodecanedioic acid; 14. octadecanoic acid; 15. dehydroabietic acid; 16. 2-palmitoyl glycerol; 17. 1-monopalmitin; 18. 2-monostearin; 19. glycerol monostearate; 20. β-amyrin; 21. 24-noroleana-3,12-diene; * contaminants.

The **colored pictorial layers** are mainly painted in yellow, blue, green and red.

The *yellow pictorial layer* (Figure 5, b) appears thin (between about 20 and 80 μm) and bright, above the white layer (c) in the cross-section and is extended on the entire surface of the coffin. It is characterized by orpiment, as already found for the yellow pictorial layer. Its tiny tabular crystals appear with characteristic golden-yellow coloration and orange under UV reflected light [34]. Regarding this layer, SEM-EDS analysis shows the

presence of As and S, whereas Py/GC-HRMS analysis reveals arsenic-based compounds (Supplementary Table S1), suggesting the use of orpiment (As_2S_3) [35]. In the same cross-section, another thin layer (b1) (about 15 μm) can be seen below the yellow one; it appears light yellow in visible light and whitish under UV light, whereas the SEM-EDS analysis does not reveal any inorganic element, so it is probably a layer of organic binder applied on the white preparatory layer (c).

The nature of the yellow pigment is verified by ATR-FTIR. The spectrum (Figure 7) shows infrared bands characteristic of orpiment (α-As_2S_3) at 378, 353 and 345 cm^{-1}, assigned to the symmetric νs (As-S) and asymmetric νas (As-S) stretching vibrations. The band at 311 cm^{-1} corresponds to a coupled stretching-bending mode, 294 cm^{-1} due to δ (S-As-S) bending vibrations, 181 cm^{-1} attributed to skeletal out-of-plane deformations, and 140 cm^{-1} attributed to inter-layer lattice phonons driven by weak van der Waals interactions [36,37].

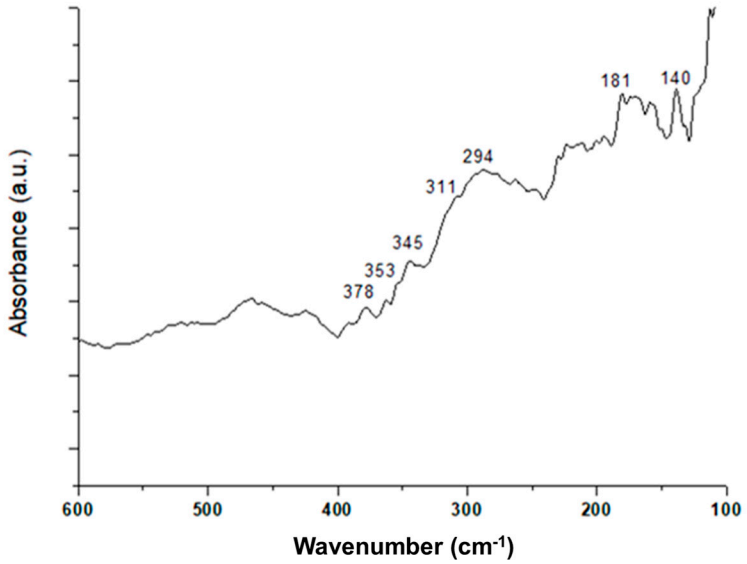


Figure 7. ATR-FIR spectrum of orpiment detected in the sample SF4.

The *blue pictorial layer* (Figure 8) is coarse-grained and up to about 140 μm in thickness. In visible light, it appears uniformly and intensely blue, while under UV light observation, it reveals blue tabular to prismatic crystals, up to approximately 40 μm in length, embedded in a glass-rich matrix [38]. These characteristics, together with the SEM-EDS distribution maps of Cu, Si and Ca, suggest the use of Egyptian blue (cuprorivaite $CaCuSi_4O_{10}$) [19,34,39,40]. The pigment grains did not exhibit clear fluorescence, whereas the matrix shows a faint yellowish fluorescence, probably associated with the presence of an organic binder.

This pigment can also be identified through ATR-FTIR analyses (Figure 9). Its characteristic peaks in the MIR and FIR regions reflect the structural dynamics of its layered silicate sheets $(Si_4O_{10})^{4-}$, coordinated to Cu^{2+} and Ca^{2+} cations. Bands at 1162 cm^{-1} νas (Si–O–Si), 1039 cm^{-1} and 1007 cm^{-1} ν (Si–O^-) characterize the main silicate sheet stretching modes, while mid-range features at 754 cm^{-1}, 660 cm^{-1}, 530 cm^{-1} and 465 cm^{-1} arise from inter-tetrahedral symmetric stretching νs (Si–O–Si), bending δ (Si–O–Si), and internal δ(O–Si–O) framework deformations. Metal-ligand interactions are observed at 601 cm^{-1} and 422 cm^{-1} ν (Cu–O coupled with silicate modes), while lower-frequency bands at 340 cm^{-1} and 279 cm^{-1} reflect Ca–O and Cu–O cation coordination dynamics, ending with a fundamental lattice phonon mode at 226 cm^{-1} [21,25,41].

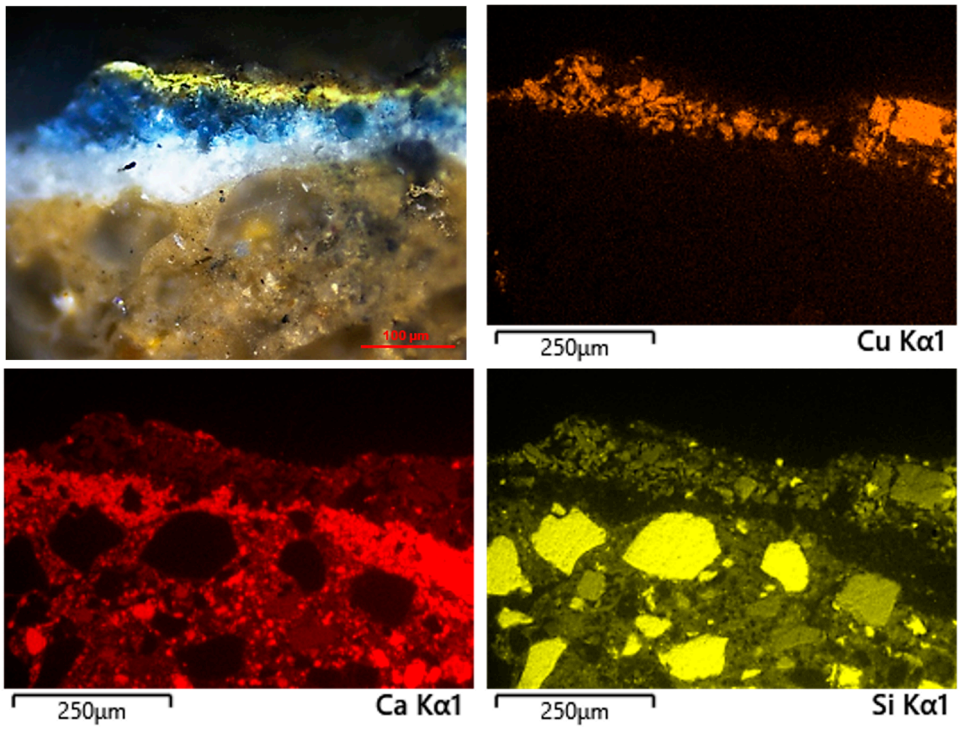


Figure 8. Sample SF4 stratigraphy observed on polished cross-section under PLM, along with SEM-EDS maps of the elements Cu, Ca and Si, detected in the same area.

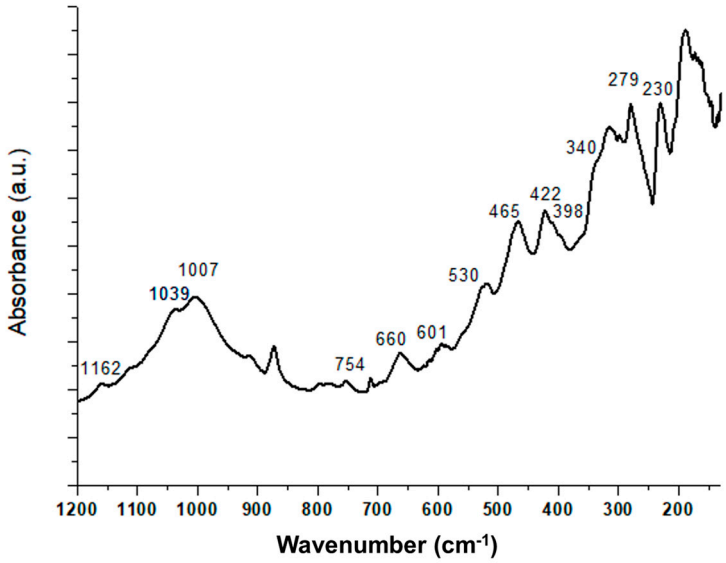


Figure 9. FTIR spectra with infrared peaks corresponding to Egyptian blue in sample SF9.

About the binder, some interesting information can be obtained from Py/GC-HRMS even if the samples are included together with the paint layer, the varnish and often the white preparatory layer. All paint film analyzed with THM–Py/GC-HRMS revealed a complex organic composition characterized by carbohydrate-derived pyrolysis products, methoxylated aromatic compounds, fatty acids, and terpenoid resin markers (Supplementary Table S1). In the pyrogram relative to the sample SF6 (Figure 10), the occurrence of furfural derivatives, cyclopentanediones, and methylated sugar-related compounds is consistent with the presence of polysaccharide-based or plant-derived materials. Methoxyphenols and methoxylated aromatic compounds, including guaiacol- and syringol-type derivatives, indicate lignin-derived or other plant-based aromatic materials.

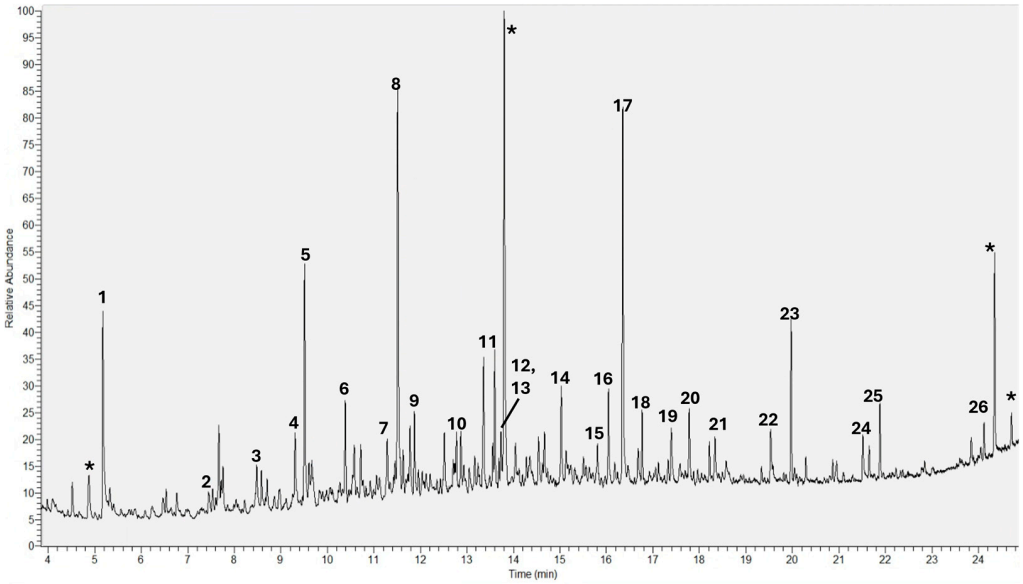


Figure 10. TIC chromatogram (T Py =500 °C, with TMAH) of the sample SF6. Legend: 1. furaldehyde; 2. dimethyl furan; 3. 3-methyl cyclopentanedione; 4. 2,4-dimethyl-1,3-cyclopentanedione; 5. 2-methoxy phenol; 6. 1,2-dimethoxy benzene; 7. 4-methoxy benzaldehyde; 8. tri-O-methyl-3-deoxy-D-threo-pentonic acid; 9. 2,6-dimethoxy phenol; 10. 1,2,3-trimethoxy benzene; 11. 1,2,4-trimethoxy benzene; 12. unidentified carbohydrate; 13. tri-O-methyl-3-deoxy-D-erythro-pentonic; 14. dimethoxy benzaldehyde; 15. nonanedioic acid; 16. dimethoxy acetophenone; 17. dimethoxy methyl ester benzoic acid; 18. 2-[(2-ethoxy-3,4-dimethyl-2-cyclohexen-1-ylidene)methyl]-Furan; 19. methyl methoxy cinnamate; 20. tetradecanoic acid; 21. 2,3,4,5-tetramethoxy benzene; 22. 3,4,5-tri-O-methyl gallic acid; 23. hexadecanoic acid; 24. 10-octaecenoic acid; 25. octadecanoic acid; 26. dehydroabietic acid; * contaminants.

The GC-HRMS analysis performed after the polysaccharide extraction procedure of the same sample (Figure 11) reveals the presence of several monosaccharides, which, in principle, could allow the identification of the type of plant gum or saccharidic material used as a binder.

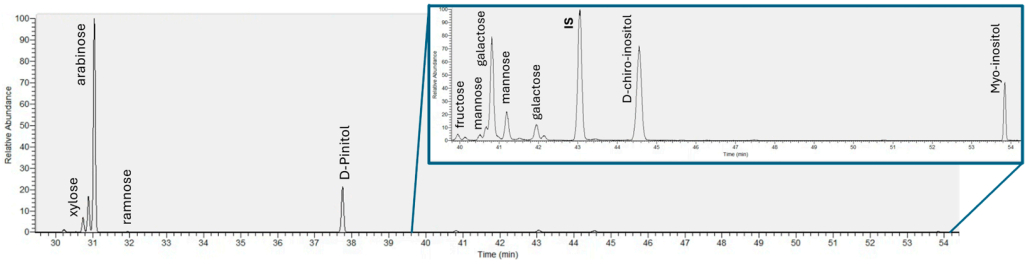


Figure 11. TIC chromatogram of the pictorial layer of the sample SF6 analyzed with the carbohydrate procedure. The monosaccharides detected and their percentages calculated are: xylose (6.82%), arabinose (89.8%), ramnose (0.89%), fructose (0.04%), mannose (2.11%) and galactose (0.34%). D-pinitol, D-chiro-inositol and myo-inositol are also identified. IS: internal standard.

The detection of arabinose, galactose, and ramnose can be related to Arabic gum, xylose and fructose to Tragacanth gum, whereas mannose is only detectable in fruit gum and not in Arabic or Tragacanth gum, although one study reported mannose in Tragacanth gum [42]. Moreover, the percentages of the monosaccharides are not consistent with those found in the literature for the gums analyzed as well [43]; therefore, the hypothesis is that the binders may have included Arabic gum but were probably a mixture of gums. The characteristic is the presence of D-pinitol and two inositol isomers (myo- and D-chiro-inositol).

The *green pictorial layer* (Figure 12), which is about 35 µm thick, has a microcrystalline and uniform texture, similar to that of malachite. The SEM-EDS analysis detected the presence of the elements Cu and Cl in the same layer, which suggests the presence of a degraded form of malachite, such as atacamite or paratacamite.

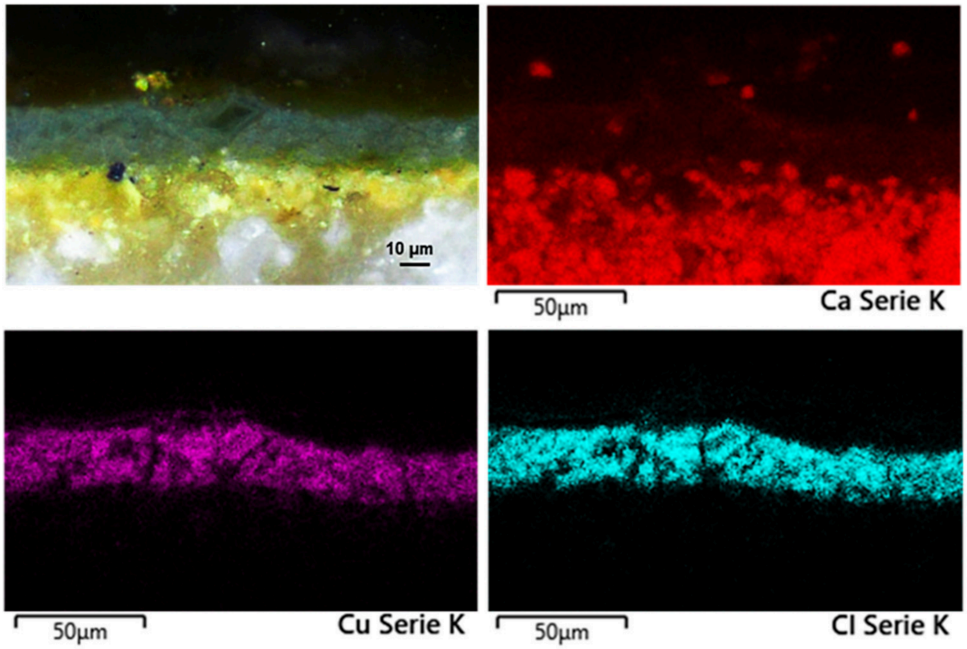


Figure 12. Sample SF5 stratigraphy observed on polished cross-section under PLM, along with SEM-EDS maps of the elements Ca, Cu and Cl.

The ATR-MIR spectrum (Figure 13) suggests the use of atacamite [34,44–46]. The bands at 3440 cm^{-1} and 3388 cm^{-1} are attributed to the intra- and intermolecular stretching vibrations ν (O–H). Their sharp, well-resolved profile arises from the ordered hydrogen-bonding network within the orthorhombic lattice, serving as a primary diagnostic tool to differentiate atacamite from trigonal paratacamite. At lower wavenumbers, the peaks at 1456 cm^{-1} and 1398 cm^{-1} correspond to in-plane Cu–O–H bending modes δ (O–H). The region below 1000 cm^{-1} features fingerprint lattice modes: bands at 989 cm^{-1} and 952 cm^{-1} are assigned to out-of-plane Cu–O–H deformations γ (O–H), while features at 920 cm^{-1}, 846 cm^{-1}, and 822 cm^{-1} arise from coupled Cu–O stretching and framework deformation modes. The FTIR spectrum of atacamite shows characteristics similar to those of paratacamite (a basic copper chloride with a trigonal crystal structure, rather than the orthorhombic structure of atacamite), but differences in the number and position of the bands make it distinguishable. In the mid-infrared (MIR) region, these structural differences result in distinct vibrational spectra, particularly evident in the hydroxyl group stretching region and in the lattice vibration region; furthermore, atacamite exhibits bands at 1399 cm^{-1} and 1458 cm^{-1}, which are absent in paratacamite.

FTIR chemical images (Figure 14) were acquired from the areas of greatest interest in order to obtain information on the spatial distribution of the chemical compounds, following single-point FTIR analyses of the sample surfaces. Specifically, FPA-FTIR chemical imaging of a cross-section of the sample SF5 was carried out on an area of 874.01 × 874.01 μm^2. Figure 11 shows the FPA-FTIR chemical maps of atacamite (copper hydroxychloride, $Cu_2Cl(OH)_3$), obtained by integrating the characteristic bands of the pigment in the range 840–995 cm^{-1} and 1320–1460 cm^{-1} [44,47,48] and of the aluminosilicates present mainly in the clay substrate, obtained by integrating the infrared bands in the range 1030–1160 cm^{-1} [48].

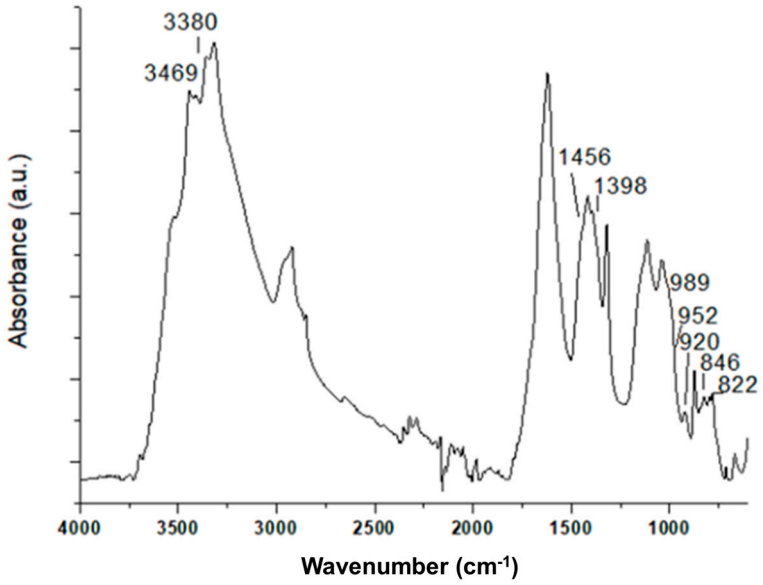


Figure 13. FTIR spectra with infrared peaks corresponding to atacamite in sample SF5.

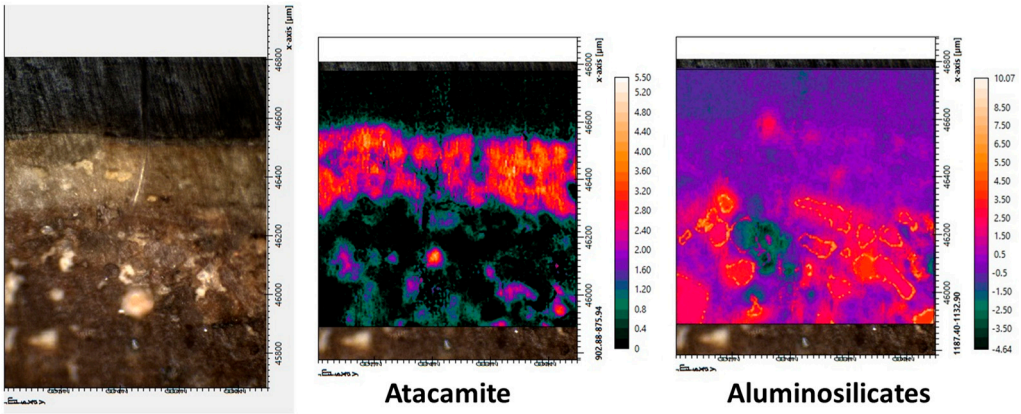


Figure 14. Image of the sample SF5 taken using the Lumos II FT-IR micro-spectrophotometer, along with FPA-FTIR chemical maps showing the spatial distribution of atacamite and the aluminosilicate components.

The *red pictorial layer* (Figure 15) is a very thin layer (of about 8 µm), with a fine and uniform texture. In this layer, SEM-EDS analyses show the presence of the elements, such as Si, Al and Fe, ascribable to the red ochre-based pigment.

The **white preparatory layer** (between about 70 and 220 µm) (Figures 5 and 16, layer (c)) is white, with a pale-yellow fluorescence under reflected UV light; while in transmitted visible light, it consists mainly of microcrystalline calcite, as confirmed by the SEM-EDS analysis. This layer is sometimes characterized by the sporadic presence of quartz and traces of gypsum.

The **brown ground layer** (Figure 16, layer (d) and detail) appears compact and coarse-grained. It is mainly composed of quartz, alkali feldspars and plagioclase, common calcareous clasts with microsparitic texture and vegetable fibers (as detailed in Figure 16), sporadic pyroxene and iron oxides, and traces of gypsum. The pyrogram relative to the brown argillaceous preparatory layer shows possible traces of a protein compound, recognized as whole egg, for the detection of pyrrole, hexadecanenitrile, octadecanenitrile, azelaic acid, palmitic acid and stearic acid [49].

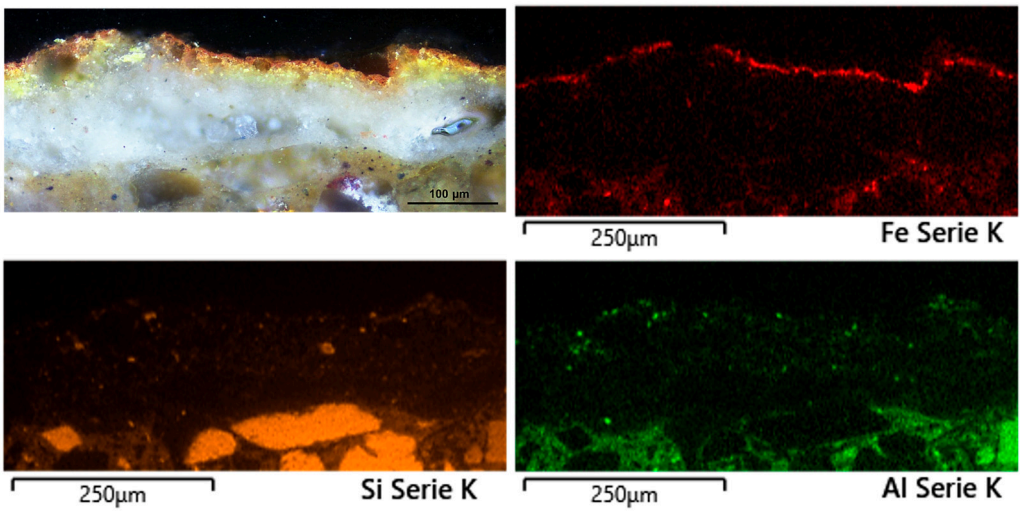


Figure 15. Sample SF9 stratigraphy observed on polished cross-section under PLM, along with SEM-EDS maps of the elements Fe, Si and Al.

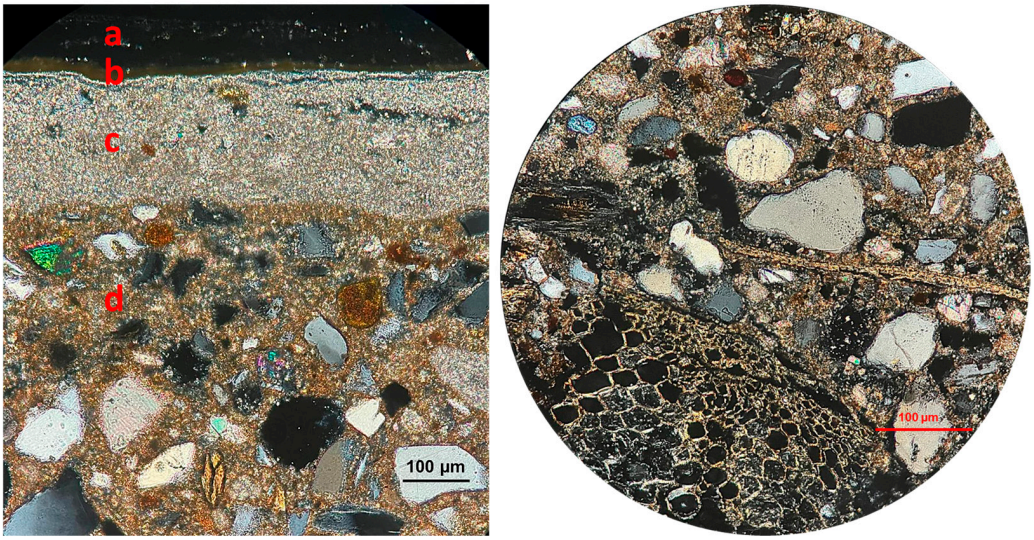


Figure 16. Micrographs of the thin cross-sections (XP): (**on the left**) preparatory layer and ground layer in sample SF1, (a) varnish layer, (b) yellow pigment layer, (c) white preparatory layer, (d) brown ground layer; (**on the right**) ground layer detail in sample SF8.

4. Discussion

The multilayered structure reflects a well-established technological procedure for the manufacture of elite Egyptian wooden coffins, in which each layer fulfilled a specific structural and aesthetic function. The recurrence of the same sequence in all analyzed cross-sections suggests the adoption of a standardized painting practice rather than local repairs or isolated interventions, supporting the technological homogeneity of the decoration.

Following on the results, the wooden coffin is covered with a mixture of coarse mud, composed mainly of quartz and feldspar grains embedded within a fine clay matrix, fully consistent with the composition of Nile alluvial mud, and applied to fill the gaps between the planks and act as a leveling surface before the application of finer preparatory coatings [19,50,51]. Chopped vegetal fibers were commonly mixed to improve cohesion and reduce shrinkage during drying [52]. The use of clay-based plasters can be traced back to the Predynastic and Early Dynastic periods. Although their quality varies, two main categories can generally be distinguished. The first consists of a coarse plaster, typically tempered with straw, whereas the second is a finer-quality material, apparently characteristic of the Theban

necropolis, which could be applied either with or without straw. This finer plaster was often used as a finishing layer over the coarser substrate. In most cases, both plaster types were subsequently coated with a layer of gypsum plaster to create a smoother and more suitable surface for painted decoration [52]. The coarse plaster is composed mainly of Nile alluvial sediment, a natural mixture of clay and sand with variable proportions, commonly containing minor amounts of calcium carbonate and, in some cases, traces of naturally occurring gypsum [20]. In contrast, the finer plaster derives from naturally deposited sediments consisting of well-mixed clay and finely divided limestone [53]. In our case, the finer plaster is not present, but the second layer is composed of a white fine calcite as a preparation layer, coherent with the Egyptian painting techniques [19,26,30,51]. The SEM-EDS analyses show a uniform distribution of Ca, confirming the predominance of calcite. Although the presence of gypsum is not revealed, the XRF analyses indicate its sporadic occurrence in association with the trace element S, more plausibly interpreted as a minor impurity naturally associated with the carbonate raw material or as a secondary product related to burial or environmental alteration, rather than as the principal constituent of the preparation layer [26]. Similar calcitic preparations [19,52] show finely ground calcite, consisting of the preferred substrate for the subsequent application of polychromy in many funerary artifacts of the New Kingdom and the Third Intermediate Period, documented until the 26th Dynasty, where this mixture was applied directly to the wood.

The thin yellow paint layer, consistently observed between the white preparation and the colored pictorial layers, represents one of the most distinctive features of the investigated stratigraphy. The MSI techniques reveal the use of arsenic-based compounds. The UVL observation shows a yellowish emission from luminescent material on the surface that presumably relates to yellow painted areas, which refers to orpiment since it gives yellow fluorescent properties [29]. This pigment is confirmed by XRF, Py/GC-HRMS and SEM-EDS analyses, thanks to the distribution of As and S in this layer, and in particular by FTIR spectroscopy. Indeed, the differentiation between arsenic sulfide pigments, such as orpiment (α-As_2S_3) and realgar (α-As_4S_4) is made possible through the identification of their characteristic vibrational bands in the mid- to far-infrared spectral regions, which reflect their distinct crystal structures. While orpiment is a layered polymer characterized by the distinctive infrared bands mentioned above (at 378 cm^{-1}, 353 cm^{-1}, 345 cm^{-1}, 311 cm^{-1}, 294 cm^{-1}, 181 cm^{-1} and 140 cm^{-1}), realgar has a distinct cage-like molecular structure. This structural difference causes realgar to exhibit intense cage-stretching bands clustered at 374 cm^{-1}, 367 cm^{-1}, 354 cm^{-1}, 341 cm^{-1}, and 328 cm^{-1}, as well as characteristic cage-bending deformations at 220 cm^{-1}, 211 cm^{-1}, and 182 cm^{-1}. Furthermore, this spectral framework allows for the easy discrimination of pararealgar (As_4S_4), a common light-induced degradation product of realgar, which is identified by its diagnostic spectral shift with primary stretching bands appearing near 347 cm^{-1}, 330 cm^{-1}, and 232 cm^{-1} [37].

Within the decorative technique of the so-called “yellow coffins”, the extensive use of this pigment assumes a particularly significant symbolic role, as the yellow background intentionally imitated the golden flesh of the gods and emphasized the solar and regenerative symbolism associated with the deceased [25,50,53,54]. It has been documented in Egypt since at least the Middle Kingdom [55] and became increasingly employed from the 18th Dynasty onwards [25,56], particularly in funerary contexts where its brilliant golden-yellow hue effectively evoked the appearance of gold [54]. Subsequently, it fell out of use owing to its limited availability and toxicity [57]. Concerning the binder, the Py/GC-HRMS, carried out on samples included together with the paint layer, the varnish and often the white preparatory layer, shows the presence of a resin component attributable to *Pistacia* resin. Recent studies have demonstrated that 28-norolean-17-en-3-one is formed when *Pistacia* resin is exposed to relatively high temperatures (above 100 °C), with its abundance

increasing as both temperature and heating duration rise. However, the compound is not stable under prolonged heating conditions or at very high temperatures and may undergo further degradation. Consequently, the detection of 28-norolean-17-en-3-one can be regarded as reliable evidence of heating processes affecting the resin. Conversely, its absence in some samples should not be interpreted as evidence that the resin was not heated, since the compound may have degraded following extended or intense thermal exposure [32].

The identification of Egyptian blue in the blue paint layers confirms the persistence of one of the most sophisticated synthetic pigments developed in antiquity [58]. It first appeared in Egypt during the 3rd millennium BC, before spreading throughout the Roman Empire [55,59–61] and remained in continuous use for its exceptional chromatic stability and its strong symbolic association with the celestial sphere, rebirth and divine protection. Optical microscopy reveals the characteristic tabular-to-prismatic morphology of the pigment particles, principally composed of Cu, Ca and Si elements detected by XRF analyses [26,27]. The SEM-EDS maps show the spatial association of the same elements, unequivocally confirming the presence of cuprorivaite [38]. While the trace elements, such as Fe, Al, S, Ti, Mn, Ni and Sn in association with the principal elements, may be due to impurities present in the quartz sand used in the synthesis of the pigment [26,27]. FTIR analyses confirmed its presence, identifying its characteristic bands in the MIR and FIR regions that show the structural dynamics of its layered silicate sheets $(Si_4O_{10})^{4-}$ coordinated to Cu^{2+} and Ca^{2+} cations. Indeed, this blue pigment can be effectively identified through Infrared Reflectography imaging because it exhibits a characteristic luminescence in the near-infrared region, approximately at 910 nm [29]. Furthermore, in IR-FC imaging, the pigment is typically rendered in red tones, allowing the recognition of blue-painted layers and providing reliable confirmation of the presence of Egyptian blue [29]. The GC-HRMS analysis, after the polysaccharide extraction procedure, reveals the presence of a type of plant gum or saccharidic material used as a binder. However, this determination is not straightforward, as degradation over time leads to changes in the chemical composition, also considering the various restoration interventions to which the coffin has been subjected over the years. The detected monosaccharides do not allow a clear attribution of the gum used; rather, the hypothesis is a mixture of gums. The high amount of characteristic D-pinitol and two inositol isomers (myo- and D-chiro-inositol) may be explained in different ways: D-pinitol has been previously identified in a kind of Acacia tree, which produces Arabic gum, specifically in Acacia nilotica, and probably indicates degradation by bacterial attack [62]. Differently, the detection of inositols can be related to vegetable tannins used for the mummification balms [63].

In the mummification balms, inositols are found together with other vegetable tannins such as o-Toluic acid, Pyroglutamic acid, 3-Phenyllactic acid, 2-furoic acid, and 4-Hydroxyacetophenone, which allows the confirmation of the use of plant extracts [64], although the carbohydrate procedure used did not specify for detecting this class of compounds. However, the chromatogram acquired after the lipidic procedure does not show these compounds. Another hypothesis of the detection of these compounds could be explained by the use of Locust bean gum, where the major compounds identified together with monosaccharides are D-pinitol, myo-inositol and D-chiro-inositol [65]. The monosaccharides contained in the Locust bean gum are mannose, galactose, arabinose, fructose and xylose that are also found in the pictorial layer, although in different percentages [43].

The GC–HRMS analysis of the paint film, subjected to a lipidic procedure, revealed the presence of a complex mixture of lipidic and resinous compounds. The occurrence of dicarboxylic acids suggests oxidative aging processes typically associated with unsaturated drying oils. However, the detection of odd-chain fatty acids, particularly pentadecanoic

acid isomers, may also indicate a minor contribution from animal fat materials, although no definitive sterol biomarkers characteristic of animal lipids were identified.

Overall, the analytical results suggest that the paint film contains an oxidized lipidic binder, most plausibly a drying oil, associated with natural resin materials, including both diterpenoid and triterpenoid resins. A minor contribution from animal fat cannot be completely excluded.

The presence of azelaic acid, considered a key marker for the oxidative degradation of unsaturated fatty acids, strongly supports the presence of an aged drying oil, most likely linseed oil, according to the established conservation science literature [49,66]. The palmitic-to-stearic acid ratio (P/S = 1.38) is consistent with values reported for historically aged linseed oil films, although partial overlap with animal fat materials cannot be entirely excluded. Moreover, although the azelaic-to-palmitic ratio (A/P = 0.02) was very low, azelaic acid was positively identified in the chromatographic profile. Quantitative evaluation of this compound was affected by coelution phenomena in the TMS-derivatized fraction, limiting the diagnostic reliability of the A/P ratio. Therefore, the interpretation was primarily based on the overall molecular profile rather than on fatty acid ratios alone.

The occurrence of azelaic acid together with other dicarboxylic acids, saturated fatty acids, and monoacylglycerols is consistent with the oxidative degradation of drying oil, particularly linseed oil. The simultaneous detection of dehydroabietic acid, β-amyrin, and 24-noroleana-3,12-diene further suggests the presence of diterpenoid and triterpenoid natural resins, indicating a complex oleo-resinous material.

The green paint layer presents a more complex interpretative framework. The bluish IR-FC response, in addition to any UV Fluorescence, shows the use of copper-based pigments, such as malachite, supported by the IR-reflected areas, where the green pigment appears dark because of its strong absorption properties in the near IR range [29]. Malachite is one of the most traditional and widely used green pigments throughout Pharaonic Egyptian history. However, the presence of Cl, detected by XRF, may suggest the pigment alteration [26,38], but it is not easy to determine whether this is the pigment originally used or a byproduct resulting from a process of deterioration. SEM-EDS analysis also confirms that the distribution maps of elements Cu and Cl overlap. The main degradation processes observed in ancient Egyptian temples have various causes [38]. In particular, Egyptian burial contexts often contain high concentrations of chloride derived from the natron used in mummification, from natural evaporite deposits, or from infiltrated saline solutions, which can be considered as major factors in the degradation of the pigment. Under these conditions, the original copper carbonate progressively converts into copper chloride hydroxide ($Cu_2Cl(OH)_3$), while largely preserving its green appearance [26,38,67].

Atacamite ($Cu_2Cl(OH)_3$), or the other polymorphs—botallackite, clinoatacamite and paratacamite—are most probably degradation products deriving from an original copper-based pigment [25,57]. An alternative mechanism involves the degradation of Egyptian blue under chloride-rich conditions [68], producing green atacamite/paratacamite together with amorphous silica through the partial dissolution of cuprorivaite [34].

However, the absence of Ca rules out this latter assumption. In the present study, the characteristic bands in FTIR analyses that differ from those of paratacamite, and are particularly evident in the regions of hydroxyl group stretching and lattice vibrations detected the predominance of atacamite. Together with the archeological burial history of the coffin, it suggests that the detected mineral is more plausibly interpreted as a secondary alteration product, rather than unequivocal evidence for the intentional use of atacamite as the original pigment.

The red paint layers are characterized by the predominance of Fe accompanied by minor amounts of Al and Si. Rather than indicating the use of purified iron oxides, the

simultaneous presence of aluminosilicate components reflects the geological origin of the pigment, in which hematite occurs naturally within clay-rich earth deposits [61]. This layer appears yellow in IR-FC, which allows us to identify the pigment as natural red ochre, including through the MSI analysis. This pigment is considered one of the most widespread in the ancient world [39], having been used from the beginning of the fifth Dynasty until the Roman period [51]. Therefore, the analytical results obtained in this study are therefore fully consistent with the established Egyptian painting tradition and further confirm the deliberate selection of naturally occurring iron-rich earth pigments for the red decorative details.

Furthermore, non-invasive analyses of the black and brown pigments were carried out. The former shows a black IR-FC response, suggesting the use of carbon-based pigment [26,28] confirmed by XRF analysis, as only the presence of Ca element was detected, probably relating to the underlying calcite-based layer [19].

The brown color associated with the blue area was found to have a high content of Cu and Ca. Although Egyptian blue is generally considered one of the most chemically stable pigments used in antiquity, being resistant to most acids, alkaline environments and prolonged light exposure, numerous archeological objects exhibit varying degrees of discoloration, ranging from slight darkening to areas that now appear dark brown or black [31]. Several mechanisms have been proposed to explain this alteration. One possibility involves the partial transformation of the original pigment into copper oxides, such as tenorite (CuO) or cuprite (Cu_2O) [52]. Alternatively, the degradation of Egyptian blue may lead to the formation of cuprite associated with copper trihydroxychlorides, resulting in brown or greenish-brown surface alterations. Some authors [31,54] further suggested that the accumulation of surface deposits or the aging of organic binding medium—some heated *Pistacia* varnishes and the Arabic gum—may also contribute to the progressive darkening of Egyptian blue, producing brownish degradation products—a phenomenon that appears to occur on the surface, while the original blue pigment remains intact beneath [54]. It is possible that pigment–binder interactions may accelerate the yellowing of the organic medium through the release of Cu^{2+} ions during the aging of Egyptian blue, further enhancing the darkened appearance of the paint layers [31]. An additional degradation pathway may involve the alteration of adjacent orpiment-rich areas, as the release of sulfur-containing degradation products can promote the deterioration of neighboring Egyptian blue, producing dark brown or greenish discoloration. In the present case, the Cu- and Ca-rich brown pigment was identified locally, within an area originally decorated with Egyptian blue. Therefore, its occurrence may suggest a possible alteration of the blue pigment; however, the specific degradation mechanism cannot be established based solely on XRF data. Further investigations are required to characterize the secondary phases involved and to clarify the processes responsible for the observed brown discoloration.

5. Conclusions

The wooden coffin, dating to the 21st Dynasty and preserved in the Egyptian Collection of the National Archaeological Museum of Florence, is an anthropoid coffin belonging to the so-called “yellow coffins” group, characterized by the predominance of a gold-yellow background in the decorative scheme, a distinctive Theban production mainly associated with high-ranking members of the Amun Temple.

The multi-analytical approach is based on non-invasive analyses—MSI and XRF—and micro-invasive analyses—OM, SEM-EDS, ATR-FTIR (MIR-FIR), FPA-FTIR and GC-HRMS, including Py/ GC-HRMS—and was performed to characterize the materials of the pictorial stratigraphy and to understand the execution techniques.

The results showed that the stratigraphy of this coffin revealed a complex and coherent multi-layered system, consisting of a coarse brown ground layer composed of Nile alluvial material tempered with vegetal fibers, which was used as a leveling substrate to fill irregularities of the wooden surface and provide mechanical support for the subsequent layers. It is followed by a fine calcite-based preparatory layer, which acted as the white ground for the application of the polychromy. The decorative sequence was completed by a widespread yellow pictorial layer containing orpiment, which played both a technological and symbolic role within the characteristic yellow background of the Egyptian coffins. The decorative areas were made using traditional Egyptian pigments, mainly including Egyptian blue, copper-based green pigment (mainly atacamite), and red ochre for the underdrawing, the red details, and the defining of the contours of the figures, as well as the carbon-based pigment for the black elements. The organic compound associated with the paint layers indicates the use of complex binder systems, involving plant gums, drying oils and natural resins, suggesting the deliberate selection and combination of different organic materials during the preparation of the pictorial films.

The uppermost alteration phenomena, particularly those affecting copper-based pigments, reflect the impact of post-depositional processes on the long-term stability of the decoration. The observed association between original materials and secondary alteration products highlights the dynamic evolution of the painted surface over time and contributes to a more comprehensive understanding of the technological choices, material selection and degradation pathways characterizing elite Egyptian funerary objects.

Supplementary Materials: The following supporting information can be downloaded at https://www.mdpi.com/article/10.3390/app162110511/s1, Figure S1: XRF analysis points 1, 2, 3 and 12 on the coffin lid; Figure S2: XRF analysis point 4 on the coffin lid; Figure S3: XRF analysis point 5 on the coffin lid; Figure S4: XRF analysis points 6, 7, 8, 10 and 14 on the inner surface of the coffin case; Figure S5: XRF analysis point 9 on the inner surface of the coffin case; Figure S6: XRF analysis points 11 and 13 on the coffin lid; Figure S7: XRF analysis points 15, 16 and 17 on the external surface of the coffin case; Table S1: list of compounds identified in samples SF1–4 and SF6–9 by THM-Py/GC-HRMS and their relative abundances.

Author Contributions: Conceptualization, G.D.F., G.G. and D.M.; methodology, G.D.F., G.G., D.M. and D.F.; software, G.D.F., G.G., D.M., M.M. and D.F.; validation, G.D.F., G.G., D.M. and A.C.; formal analysis, G.D.F., G.G., D.M., M.M. and D.F.; investigation, G.D.F., G.G., D.M. and D.F.; resources, G.G., D.M. and A.C.; data curation, G.D.F., G.G., D.M., M.M. and D.F.; writing—original draft preparation, G.D.F., G.G., D.M., D.F. and A.C.; writing—review and editing, G.D.F., G.G., D.M., D.F. and A.C.; visualization, G.D.F., G.G., D.M., D.F., M.M. and A.C.; supervision, G.D.F. and G.G. All authors have read and agreed to the published version of the manuscript.

Funding: GC-HRMS, FTIR spectroscopy, and SEM-EDS analyses were conducted at the FIXLAB node of the European Research Infrastructure (E-RIHS) located in Lecce, Italy, at CNR-ISPC. The laboratory was provided with a grant from MIUR, Italy through the SHINE (Strengthening the Italian Node of E-RIHS) Project (PIR01_00016, PON IR 2014-2020).

Institutional Review Board Statement: Not applicable.

Informed Consent Statement: Not applicable.

Data Availability Statement: The original contributions presented in this study are included in the article/Supplementary Material. Further inquiries can be directed to the corresponding authors.

Acknowledgments: The authors want to thank Mario Iozzo, then Director of the National Archaeological Museum of Florence, for planning the restoration program, which included the coffin investigated in this study.

Conflicts of Interest: Author Davide Melica was employed by Consulenza e Diagnostica per il Restauro e la Conservazione Enterprise. The remaining authors declare that the research was conducted in the absence of any commercial or financial relationships that could be construed as a potential conflict of interest.

References

1. Consonni, A. The Egyptian Collection of the Museo Archeologico Nazionale in Florence. In *Memory is Our Future*; Greco, C., Ed.; Panini Editore: Modena, Italy, 2024; pp. 162–169.
2. Niwinski, A. *21st Dynasty Coffins from Thebes: Chronological and Typological Studies*; Verlag Philipp von Zabern: Darmstadt, Germany, 1988.
3. Taylor, J.H. *Egyptian Coffins*; Shire: Princes Risborough, UK, 1989.
4. van Walsem, R. *The Coffin of Djedmonthuiufankh in the National Museum of Antiquities at Leiden*; Nederlands Instituut voor het Nabije Oosten: Leiden, The Netherlands, 1997.
5. Aston, D.A. *Burial Assemblages of Dynasty 21–25: Chronology, Typology, Developments*; Verlag der Österreichischen Akademie der Wissenschaften: Wien, Austria, 2009.
6. Sousa, R.; Amenta, A.; Cooney, K.M. *Bab El-Gasus in Context: Rediscovering the Tomb of the Priests of Amun*; Sousa, R., Amenta, A., Cooney, K.M., Eds.; L'Erma di Bretschneider: Rome, Italy, 2021.
7. *The Tomb of the Priests of Amun*; Sousa, R., Ed.; BRILL: Leiden, The Netherlands, 2019.
8. Rougerio, S.; Zarli, M. Coffin Set of an Anonymous Woman (A.60). In *The Tomb of the Priests of Amun*; Sousa, R., Ed.; BRILL: Leiden, The Netherlands, 2018; pp. 236–322.
9. Cooney, K.M. Coffin Reuse in 21st Dynasty: A Case Study of the Bab El-Gasus Coffins in the Egyptian Museum of Florence. In *The Tomb of the Priests of Amun: Burial Assemblages in the Egyptian Museum of Florence*; Sousa, R., Ed.; Brill: Leiden, The Netherlands, 2018; pp. 492–514.
10. Cooney, K.M. *The Cost of Death: The Social and Economic Value of Ancient Egyptian Funerary Art in the Ramesside Period*; Egyptologische Uitgaven: Leiden, The Netherlands, 2007.
11. Cooney, K.M. Patterns of Coffin Reuse from Dynasties 19 to 22. In *Ancient Egyptian Coffins: Past-Present-Future*; Dawson, J., Strudwick, H., Eds.; Oxbow Books: Oxford, UK, 2018; pp. 96–108.
12. Giachi, G.; Guidotti, M.C.; Lazzeri, S.; Macchioni, N.; Sozzi, L. Wood Identification of Some Coffins from the Necropolis of Thebes Held in the Collection of the Egyptian Museum in Florence. *J. Cult. Herit.* **2021**, *47*, 34–42. [CrossRef]
13. Amenta, A.; Guichard, H. *Proceedings First Vatican Coffin Conference: 19–22 June 2013*; Edizioni Musei Vaticani: Città del Vaticano, Italy, 2017.
14. Strudwick, H.; Dawson, J. *Ancient Egyptian Coffins: Past-Present-Future*; Oxbow Books: Oxford, UK, 2018.
15. Weiss, L.; te Leiden, R.V.O. *The Coffins of the Priests of Amun. Egyptian Coffins from the 21st Dynasty in the Collection of the National Museum of Antiquities in Leiden*; Sidestone Press: Leiden, The Netherlands, 2018.
16. *Proceedings Second Vatican Coffin Conference*; Amenta, A., Iob, A., Eds.; Edizioni Musei Vaticani: Città del Vaticano, Italy, 2025.
17. Andreotti, A.; Bonaduce, I.; Colombini, M.P.; Gautier, G.; Modugno, F.; Ribechini, E. Combined GC/MS Analytical Procedure for the Characterization of Glycerolipid, Waxy, Resinous, and Proteinaceous Materials in a Unique Paint Microsample. *Anal. Chem.* **2006**, *78*, 4490–4500. [CrossRef] [PubMed]
18. Moretti, P.; Germinario, G.; Doherty, B.; van der Werf, I.D.; Sabbatini, L.; Mirabile, A.; Sgamellotti, A.; Miliani, C. Disclosing the Composition of Historical Commercial Felt-Tip Pens Used in Art by Integrated Vibrational Spectroscopy and Pyrolysis-Gas Chromatography/Mass Spectrometry. *J. Cult. Herit.* **2019**, *35*, 242–253. [CrossRef]
19. Abdelmoniem, A.M.; Mahmoud, N.; Ahmed ABDEL-FATAH, M.; Mohamed, S.; Badr, N.M. Multi Analytical Techniques of Anthropoid Wooden Coffin from Egypt's Late Period. *Int. J. Conserv. Sci.* **2022**, *13*, 1087–1100.
20. Pagès-Camagna, S.; Laval, E.; Vigears, D.; Duran, A. Non-Destructive and in Situ Analysis of Egyptian Wall Paintings by X-Ray Diffraction and X-Ray Fluorescence Portable Systems. *Appl. Phys. A Mater. Sci. Process.* **2010**, *100*, 671–681. [CrossRef]
21. Abdrabou, A.; Abdallah, M.; Shaheen, I.A.; Kamal, H.M. Investigation of an Ancient Egyptian Polychrome Wooden Statuette by Imaging and Spectroscopy. *Int. J. Conserv. Sci.* **2018**, *9*, 39–54.
22. Aldrovandi, A.; Bellucci, R.; Bertani, D.; Buzzegoli, E.; Cetica, M.; Kunzelman, D. La Ripresa in Infrarosso Falso Colore. *Nuove Tec. DI Util.* **1993**, *5*, 94–98.
23. Cosentino, A. Identification of Pigments by Multispectral Imaging; a Flowchart Method. *Herit. Sci.* **2014**, *2*, 8. [CrossRef]
24. Matteini, M.; Moles, A.; Tiano, P. L'infrarosso Colore Nell'indagine Dei Dipinti. *LE Sci.* **1980**, *142*, 40–48.
25. Bonizzoni, L.; Bruni, S.; Gargano, M.; Guglielmi, V.; Zaffino, C.; Pezzotta, A.; Pilato, A.; Auricchio, T.; Delvaux, L.; Ludwig, N. Use of Integrated Non-Invasive Analyses for Pigment Characterization and Indirect Dating of Old Restorations on One Egyptian Coffin of the XXI Dynasty. *Microchem. J.* **2018**, *138*, 122–131. [CrossRef]

26. Atwa, D.M.; Hussein, R.K.; Mohamed, I.F.; Ibrahim, S.; Abdullah, E.; Omar, G.; Ibrahim, M.A.; Refaat, A. Structural and Chemical Degradation of Archeological Wood: Synchrotron XRD and FTIR Analysis of a 26th Dynasty Egyptian Polychrome Wood Statuette. *Polymers* **2026**, *18*, 258. [CrossRef] [PubMed]
27. Dariz, P.; Schmid, T. Trace Compounds in Early Medieval Egyptian Blue Carry Information on Provenance, Manufacture, Application, and Ageing. *Sci. Rep.* **2021**, *11*, 11296. [CrossRef] [PubMed]
28. Bonizzoni, L.; Bruni, S.; Guglielmi, V.; Milazzo, M.; Neri, O. Field and Laboratory Multi-Technique Analysis of Pigments and Organic Painting Media from an Egyptian Coffin (26th Dynasty). *Archaeometry* **2011**, *53*, 1212–1230. [CrossRef]
29. Moustafa, M.; Abdallah, M.; Abdrabou, A.; Kamal, H.M. A Multi-Analytical Investigation of an Ancient Egyptian Painted Wooden Coffin from the Late Period. *Int. J. Conserv. Sci.* **2022**, *13*, 3–14.
30. Scott, D.A. A Review of Ancient Egyptian Pigments and Cosmetics. *Stud. Conserv.* **2016**, *61*, 185–202. [CrossRef]
31. Daniels, V.; Stacey, R.; Middleton, A. The Blackening of Paint Containing Egyptian Blue. *Stud. Conserv.* **2004**, *49*, 217–230. [CrossRef]
32. Tamburini, D.; Fulcher, K.; Briggs, L.; von Aderkas, N.; Pulak, C.; Stacey, R. Advances in the Characterisation and Identification of Mastic (*Pistacia* sp.) Resin in Archaeological Samples by GC-QToF-MS. *RSC Adv.* **2024**, *14*, 836–854. [CrossRef] [PubMed]
33. Davara, J.; Jambrina-Enríquez, M.; Rodríguez de Vera, C.; Herrera-Herrera, A.V.; Mallol, C. Pyrotechnology and Lipid Biomarker Variability in Pine Tar Production. *Archaeol. Anthropol. Sci.* **2023**, *15*, 133. [CrossRef]
34. Giménez, J. Egyptian Blue and/or Atacamite in an Ancient Egyptian Coffin. *Int. J. Conserv. Sci.* **2015**, *6*, 747–749.
35. Sogliani, F. La Ceramica Ed i Vetri Medievali Dagli Scavi Del Rione Terra Di Pozzuoli: Aspetti e Problemi Di Circolazione e Di Produzione Nella Campania Costiera Tra XII e XIV Secolo. In *Archeologia Medievale: Cultura Materiale, Insediamenti, Territorio: XXVII, 2000*; Torrossa: Florence, Italy, 2000; pp. 391–406.
36. Karr, C.; Kovach, J.J. Far-Infrared Spectroscopy of Minerals and Inorganics. *Appl. Spectrosc.* **1969**, *23*, 219–223. [CrossRef]
37. Ogalde, J.P.; Salas, C.; Lara, N.; Leyton, P.; Paipa, C.; Campos-Vallette, M.; Arriaza, B. Multi-Instrumental Identification of Orpiment in Archaeological Mortuary Contexts. *J. Chil. Chem. Soc.* **2014**, *59*, 2571–2573. [CrossRef]
38. Marey Mahmoud, H.H. Microanalysis of Blue Pigments from the Ptolemaic Temple of Hathor (Thebes), Upper Egypt: A Case Study. *Surf. Interface Anal.* **2012**, *44*, 1271–1278. [CrossRef]
39. Brecoulaki, H.; Fiorin, E.; Vigato, P.A. The Funerary Klinai of Tomb 1 from Amphipolis and a Sarcophagus from Ancient Tragilos, Eastern Macedonia: A Physico-Chemical Investigation on the Painting Materials. *J. Cult. Herit.* **2006**, *7*, 301–311. [CrossRef]
40. Pagès-Camagna, S.; Colinart, S. The Egyptian Green Pigment: Its Manufacturing Process and Links to Egyptian Blue. *Archaeometry* **2003**, *45*, 637–658. [CrossRef]
41. Lombardi, C.A.; Comite, V.; Fermo, P.; Bergomi, A.; Trombino, L.; Guglielmi, V. A Multi-Analytical Approach for the Characterisation of Pigments from an Egyptian Sarcophagus Cover of the Late Dynastic Period: A Case Study. *Sustainability* **2023**, *15*, 2002. [CrossRef]
42. Lluveras-Tenorio, A.; Mazurek, J.; Restivo, A.; Colombini, M.P.; Bonaduce, I. Analysis of Plant Gums and Saccharide Materials in Paint Samples: Comparison of GC-MS Analytical Procedures and Databases. *Chem. Cent. J.* **2012**, *6*, 115. [CrossRef] [PubMed]
43. Lluveras-Tenorio, A.; Mazurek, J.; Restivo, A.; Colombini, M.P.; Bonaduce, I. The Development of a New Analytical Model for the Identification of Saccharide Binders in Paint Samples. *PLoS ONE* **2012**, *7*, e49383. [CrossRef] [PubMed]
44. Catelli, E.; Sciutto, G.; Prati, S.; Jia, Y.; Mazzeo, R. Characterization of Outdoor Bronze Monument Patinas: The Potentialities of near-Infrared Spectroscopic Analysis. *Environ. Sci. Pollut. Res.* **2018**, *25*, 24379–24393. [CrossRef] [PubMed]
45. Martens, W.; Frost, R.L.; Williams, P.A. Raman and Infrared Spectroscopic Study of the Basic Copper Chloride Minerals-Implications for the Study of the Copper and Brass Corrosion and "Bronze Disease". *Neues Jahrb. Für Mineral.-Abh.* **2003**, *178*, 197–215. [CrossRef]
46. De Haro, A.; Córdova, M.; Rua Landa, C.; Huck-Iriart, C.; Siracusano, G.; Maier, M.S.; Tomasini, E. Methodologies for the Characterization and Identification of Natural Atacamite as a Pigment in Andean Colonial Painting. *Heritage* **2023**, *6*, 5116–5129. [CrossRef]
47. Iannaccone, R.; Giuliani, S.; Lenzi, S.; Franceschini, M.M.N.; Vettori, S.; Salvadori, B. A Cippus from Turris Libisonis: Evidence for the Use of Local Materials in Roman Painting on Stone in Northern Sardinia. *Minerals* **2024**, *14*, 1040. [CrossRef]
48. Derrick, M.R.; Stulik, D.; Landry, J.M. *Infrared Spectroscopy in Conservation Science. Scientific Tools for Conservation*; Getty Conservation Institute: Los Angeles, CA, USA, 1999.
49. Bonaduce, I.; Andreotti, A. Py-GC/MS of Organic Paint Binders. In *Organic Mass Spectrometry in Art and Archaeology*; Wiley: Hoboken, NJ, USA, 2009; pp. 303–326.
50. Afifi, H.; Hamed, S.A.E.K.M.; Mohamedy, S.; Dawod, M. A Dating Approach of a Refundable Wooden Egyptian Coffin Lid. *Sci. Cult.* **2019**, *5*, 15–22. [CrossRef]
51. Salem, R.; Owais, A.; Salama, R. The Conservation of an Egyptian Polychrome Wood Coffin from Late Period. *Egypt. J. Archaeol. Restor. Stud.* **2016**, *6*, 23–37. [CrossRef]
52. Lucas, A.; Harris, J.R. *Ancient Egyptian Materials and Industries*, 4th ed.; Dover Pubns: Mineola, NY, USA, 2005.

53. Brunel-Duverger, L.; Doublet, C.; Laval, E.; Brodie-Linder, N.; Pages-Camagna, S. Contribution from SEM Studies in the Understanding of Degradation Mechanisms of Copper Green Pigments from the Louvre Museum's 21st Dynasty Egyptian Coffins. *Microsc. Microanal.* **2018**, *24*, 2126–2127. [CrossRef]
54. Van der Perre, A.; Boschloos, V.; Hameeuw, H.; Braekmans, D. A Complementary Integrated Approach Using Non-Destructive Optical and X-Ray Methodologies for Pigment Characterisation on an Ancient Egyptian Coffin. *Eur. Phys. J. Plus* **2025**, *140*, 428. [CrossRef]
55. Badr, N.M.; Ali, M.F.; El Hadidi, N.M.N.; Naeem, G.A. Identification of Materials Used in a Wooden Coffin Lid Covered with Composite Layers Dating Back to the Ptolemaic Period in Egypt. *Conserv. Patrim.* **2018**, *29*, 11–24. [CrossRef]
56. Chiavari, G.; Fabbri, D.; Galletti, G.C.; Mazzeo, R. Use of Analytical Pyrolysis to Characterize Egyptian Painting Layers. *Chromatographia* **1995**, *40*, 594–600. [CrossRef]
57. Franquelo, M.L.; Duran, A.; Herrera, L.K.; Jimenez de Haro, M.C.; Perez-Rodriguez, J.L. Comparison between Micro-Raman and Micro-FTIR Spectroscopy Techniques for the Characterization of Pigments from Southern Spain Cultural Heritage. *J. Mol. Struct.* **2009**, *924–926*, 404–412. [CrossRef]
58. Baraldi, P.; Bondioli, F.; Fagnano, C.; Ferrari, A.M.; Tinti, A.; Vinella, M. Study of the Vibrational Spectrum of Cuprorivaite. *Ann. Chim.* **2001**, *91*, 679–692. [PubMed]
59. Mazzocchin, G.A.; Rudello, D.; Bragato, C.; Agnoli, F. A Short Note on Egyptian Blue. *J. Cult. Herit.* **2004**, *5*, 129–133. [CrossRef]
60. Riederer, J. Egyptian Blue. In *Artists' Pigments: A Handbook of Their History and Characteristics*; FitzHugh, E.W., Ed.; National Gallery of Art: Washington, DC, USA, 1997; Volume 3, pp. 23–45.
61. Marey Mahmoud, H.H. Investigations by Raman Microscopy, ESEM and FTIR-ATR of Wall Paintings from Qasr El-Ghuieta Temple, Kharga Oasis, Egypt. *Herit. Sci.* **2014**, *2*, 18. [CrossRef]
62. Fulcher, K.; Spencer, N.; Budka, J.; Stacey, R.J. Polysaccharide Paint Binding Media at Two Pharaonic Settlements in Nubia. *Heritage* **2022**, *5*, 2028–2040. [CrossRef]
63. Mejanelle, P.; Bleton, J.; Goursaud, S.; Tchapla, A. Identification of Phenolic Acids and Inositols in Balms and Tissues from an Egyptian Mummy. *J. Chromatogr. A* **1997**, *767*, 177–186. [CrossRef] [PubMed]
64. Barberis, E.; Manfredi, M.; Ferraris, E.; Bianucci, R.; Marengo, E. Non-Invasive Paleo-Metabolomics and Paleo-Proteomics Analyses Reveal the Complex Funerary Treatment of the Early 18th Dynasty Dignitary NEBIRI (QV30). *Molecules* **2022**, *27*, 7208. [CrossRef] [PubMed]
65. Christou, C.; Poulli, E.; Yiannopoulos, S.; Agapiou, A. GC–MS Analysis of D-Pinitol in Carob: Syrup and Fruit (Flesh and Seed). *J. Chromatogr. B* **2019**, *1116*, 60–64. [CrossRef] [PubMed]
66. Colombini, M.P.; Modugno, F.; Giacomelli, M.; Francesconi, S. Characterisation of Proteinaceous Binders and Drying Oils in Wall Painting Samples by Gas Chromatography–Mass Spectrometry. *J. Chromatogr. A* **1999**, *846*, 113–124. [CrossRef]
67. Schiegl, S.; Weiner, K.L.; Goresy, A. El Discovery of Copper Chloride Cancer in Ancient Egyptian Polychromic Wall Paintings and Faience: A Developing Archaeological Disaster. *Sci. Nat.* **1989**, *76*, 393–400. [CrossRef]
68. Moussa, A.; Badawy, M.; Saber, N. Chromatic Alteration of Egyptian Blue and Egyptian Green Pigments in Pharaonic Late Period Tempera Murals. *Sci. Cult.* **2021**, *7*, 1. [CrossRef]

Disclaimer/Publisher's Note: The statements, opinions and data contained in all publications are solely those of the individual author(s) and contributor(s) and not of MDPI and/or the editor(s). MDPI and/or the editor(s) disclaim responsibility for any injury to people or property resulting from any ideas, methods, instructions or products referred to in the content.